Peptide-Directed PdAu Nanoscale Surface Segregation: Toward Controlled Bimetallic Architecture for Catalytic Materials

Nicholas M. Bedford,[1*] Allison R. Showalter,[2] Taylor J. Woehl,[1] Zak E. Hughes,[3] Sungsik Lee,[4] Benjamin Reinhart,[4] S. Piril Ertem,[5] E. Bryan Coughlin,[5] Yang Ren,[4] Tiffany R. Walsh,[3] Bruce A. Bunker[2]

[1] *Applied Chemical and Materials Division, National Institute of Standards and Technology, Boulder, CO 80305 USA*

[2] *Department of Physics, University of Notre Dame, Notre Dame, IN 46556 USA*

[3] *Institute for Frontier Materials, Deakin University, Geelong, Vic. 3216 Australia*

[4] *X-ray Sciences Division, Argonne National Laboratory, Argonne, IL 60439 USA*

[5] *Department of Polymer Science and Engineering, University of Massachusetts Amherst, Amherst, MA, 01003 USA*

Abstract

Bimetallic nanoparticles are of immense scientific and technological interest given the synergistic properties observed when mixing two different metallic species at the nanoscale. This is particularly prevalent in catalysis, where bimetallic nanoparticles often exhibit improved catalytic activity and durability over their monometallic counterparts. Yet despite intense research efforts, little is understood regarding how to optimize bimetallic surface composition and structure synthetically using rational design principles. Recently, it has been demonstrated that peptide-enabled routes for nanoparticle synthesis result in materials with sequence-dependent catalytic properties, providing an opportunity for rational design through sequence manipulation. In this study, bimetallic PdAu nanoparticles are synthesized with a small set of peptides containing known Pd and Au binding motifs. The resulting nanoparticles were extensively characterized using high-resolution scanning transmission electron microscopy, X-ray absorption spectroscopy and high-energy X-ray diffraction coupled to atomic pair distribution function analysis. Structural information obtained from synchrotron radiation methods were then used to generate model nanoparticle configurations using reverse Monte Carlo simulations, which illustrate sequence-dependence in both surface structure and surface composition. Replica exchange solute tempering molecular dynamic simulations were also used to predict the modes of peptide binding on monometallic surfaces, indicating that different sequences bind to the metal interfaces via different mechanisms. As a testbed reaction, electrocatalytic methanol oxidation experiments were performed, wherein differences in catalytic activity are clearly observed in materials with identical bimetallic composition. Taken together, this study indicates that peptides could be used to arrive at bimetallic surfaces with enhanced catalytic properties, which could be leveraged for rational bimetallic nanoparticle design using peptide-enabled approaches.

Introduction

Metallic nanoparticles demonstrate great utility in catalytic applications due to the high surface area to volume ratios inherent to nanoscale materials. Given current energy and environmental challenges, extensive research efforts have focused on the generation of highly active catalytic nanoparticles, particularly for applications concerning alternative energy-based technologies such as (photo)electrochemical fuel cells and biomass refinement processes.[1, 2] Strategies for improving the catalytic activity of metallic nanoparticles involve the optimization of nanoparticle composition, shape, and/or structure, wherein the ability to predictably control the structural motifs present on the nanoparticle surface at the atomic scale will likely advance the discovery of materials with enhanced catalytic properties. Along these lines, the development of bimetallic nanoparticles aims to improve catalytic activity as compared with their corresponding monometallic counterparts by introducing synergistic improvements in catalytic properties arising from unique electronic and geometric effects found in bimetallic nanoparticles.[3, 4] Yet despite increased research efforts focused on bimetallic nanoparticle synthesis, there is a comparatively smaller body of literature focused on understanding bimetallic nanoparticle composition and surface segregation as a function of capping agent-bimetallic interactions during and after synthesis.[5, 6] More commonly, current studies have largely focused on the reorganization of surface atoms during catalysis due to reaction conditions such as applied electrical bias, changes in temperature, and the presence of small molecule reagents and products during catalytic reactions.[7-9] Such efforts demonstrate the need to elucidate atomic-scale structural evolution during catalysis, but perhaps equally important, illustrate the possibility of synthetically tuning bimetallic surface composition through nanoparticle-ligand interactions. Ligand-induced structural dependences have been previously reported,[5, 6] yet concise design strategies for achieving controlled bimetallic composition/structure for catalysts optimization have yet to be realized. As such, bimetallic nanocatalysts are often synthesized using trial-and-error approaches that cannot be readily translated across a variety of materials systems. In order to create new catalytic materials with enhanced properties in a non-Edisonian

fashion, rational synthetic strategies are needed that are rooted in the fundamental understanding of atomic-scale structure/function relationships.

An emerging method for nanoparticle synthesis and assembly is the use of biomolecule-directed techniques.[10, 11] Performed under energy- and environmentally-friendly conditions (aqueous media, ambient temperature and pressure), biomolecules such as DNA, proteins, and peptides have been used to assemble and/or synthesize a wide range of nanoscale materials.[12-20] In the context of catalysis, peptide-enabled synthetic strategies have been recently used to create nanoparticle catalysts that operate under aqueous conditions and low catalyst loading.[18, 20] Additionally, these materials demonstrate catalytic property modulation that is dependent on the primary sequence of the capping peptide, which is non-covalently (physically) adsorbed onto the nanoparticle surface.[21-23] Such observations suggest bio-inspired routes can be used to optimize catalytic properties for bimetallic systems, but can only be fully realized if sequence-dependent structure/function relationships are better understood. We have recently reported on developing such relationships using atomic-scale structural methods for peptide-capped monometallic catalysts,[24, 25] wherein the presence of strongly-adsorbing residues in the peptide sequence drive formation of disordered catalytic surfaces. Such strategies for monometallic systems are likely adaptable to bimetallic nanoparticles, while also providing a means to modulate surface composition through complex interactions at the biotic/abiotic interface. Examples of peptide-enabled bimetallic nanoparticles are limited,[26-29] and have not to date explored the possible utility of sequence modification to direct and manipulate the surface composition and/or structural order of the catalyst.

In this contribution, we have created small (~2 nm) PdAu nanoparticles using a set of peptide sequences that incorporate known binding motifs for Pd and Au. These nanoparticles were extensively characterized using high-resolution scanning transmission electron microscopy (HR-STEM), X-ray absorption fine-structure spectroscopy (XAFS), and high-energy X-ray diffraction (HE-XRD) coupled to atomic pair distribution function (PDF) analysis. Modeling of XAFS and atomic PDF datasets provide structural information over varying length scales to generate experimentally-derived nanoparticle configurations, which were found to exhibit sequence-dependent Pd surface segregation.

To assess sequence-dependent structure/function relationships, electrochemical methanol oxidation was performed as a model reaction. In addition, state-of-the-art replica exchange with solute tempering[30, 31] molecular dynamics (REST-MD) simulations were performed at peptide-monometallic (Pd^0 and Au^0) interfaces to elucidate the atomic-scale phenomena that drive the peptide-induced phase separations in bimetallic nanoparticles. Overall, our findings demonstrate the capability to control surface composition and structural order in bimetallic nanoparticles via the choice of peptide sequence, potentially leading to new approaches to rationally optimize catalytic properties through predictable manipulation of biotic/abiotic interactions at the bimetallic nanoparticle surface.

Results and Discussion

To evaluate the capability of exploiting interactions at the biotic/abiotic interface as a means to control bimetallic nanoparticle surface composition and structural order, a set of peptide-enabled PdAu nanoparticles were synthesized. PdAu was chosen as a model system given the comparatively large amount of literature on peptide-Pd/Au interactions[23-25, 32-34] and the well-established catalytic property enhancements observed in PdAu alloys.[26, 35] The Pd4 peptide (TSNAVHPTLRHL), derived from M13 phage display experiments on bulk polycrystalline Pd,[18] has been suggested to non-covalently bind to Pd through the histidine residues at the 6 and 11 positions in the peptide.[32] Further sequence modifications in Pd4 at the 6 and 11 positions with alanine and/or cysteine yield differences in catalytic properties,[22, 23] which we recently discovered was attributed to sequence-driven surface disorder in Pd.[24] Similarly, the AuBP1 peptide (WAGAKRLVLRRE), discovered by FliTrx selection methods on Au surfaces,[36] has been extensively studied with using both computational and experimental methods.[34, 36, 37] Recent REST-MD simulations [34, 37] of AuBP1 adsorbed at the aqueous Au (111) interface have found that Trp, and to a lesser extent Arg, feature strong non-covalent interactions with Au interfaces. Leveraging this knowledge of Pd and Au interactions with Pd4 and AuBP1 peptides, we designed a hybrid peptide, termed H1 (WAGAKRHPTLRHL), that contains strong anchoring motifs from the N-terminal half of AuBP1[34] and the C-terminal half of Pd4[32].

Using the AuBP1, Pd4, and H1 sequences, PdAu nanoparticles were synthesized using an adapted method for peptide-capped Au nanoparticles (see the experimental section for more details).[21] PdAu nanoparticles were synthesized at 3:1, 1:1, and 1:3 Pd:Au ratios, along with pure monometallic Au and Pd nanoparticles. STEM images show nanoparticle ~2 nm in size were synthesized for all bimetallic ratios and peptides, as highlighted for 1:3 Pd:Au nanoparticles capped with the AuBP1 peptide in Figure 1 (see Figure S1-S3, for images for each nanoparticle). AuBP1 capped 1:3 Pd:Au nanoparticles are 2.1 ± 0.9 nm in size (Figure 1a & 1b), and demonstrate ordered domains in high-angle annular dark field-STEM (HAADF-STEM) imaging. While such results would suggest nanocrystalline order, we stress that HAADF-STEM imaging is a 2D representation of a 3D nanoparticle structure and only reveal crystalline order in the core of the nanoparticle and not surface structure. Indeed, our previous HR-TEM work on peptide-capped Pd nanoparticles show atomic order in the core of the nanoparticles, but the images could not be used to glean structural information on the nanoparticle surface.[24] For sizing aspect ratio analysis on all bimetallic nanoparticles, see Table S1. STEM energy dispersive x-ray spectroscopy (STEM-EDS) elemental mapping was performed (Figure 1d) for both Au and Pd (Figure 1e and 1f) to better understand the spatial distribution of Pd and Au in the nanoparticles. Figure 1e illustrates concentrated Au signal toward the center of each nanoparticle, while the Pd signal (Figure 1f) is more diffuse in nature and spread over a larger area than the Au for each particle. Such an arrangement of EDS intensities suggests that Pd resides predominantly on the surface of the nanoparticles in these materials, although emphatic evidence based solely on EDS mapping is hard to ascertain for nanoparticles of this size. In addition, the EDS signal from Pd and Au is uniform across all nanoparticles, qualitatively indicating a lack of chemical segregation in the nanoparticles.

Synchrotron radiation characterization methods were implemented to understand the influence of peptide sequence on the resulting structure of the peptide-capped nanoparticles. First, we used XAFS to probe local structure and chemistry in an element specific fashion. XAFS is an established method for understanding local bimetallic nanoparticle structure through the identification of metal-metal coordination numbers (CNs).[38] In this instance, XAFS experiments around the Pd K-edge and Au L_3-edge can

provide Pd-Pd, Pd-Au, Au-Pd, and Au-Au CNs that are paramount in understanding the influence of peptide sequence on local atomic-scale bimetallic arrangements. X-ray energies were scanned from 200 eV below to 900 eV above each element's absorption edge (Figure S4). The X-ray absorption near-edge structure (XANES) spectra around the Au L_3-edge (11.92 keV) for PdAu nanoparticles made with AuBP1, H1, and Pd4 all indicate the Au atoms are zerovalent as evident by similarity in XANES features to that of a reference Au foil (Figure S5). Similarly, XANES features around the Pd K-edge (24.35 keV) indicate that the Pd in the PdAu nanoparticles is largely metallic, as compared to bulk Pd. Monometallic Pd nanoparticles, conversely, exhibit XANES features that are more akin to oxidized Pd. Note that such instances have been previously observed in peptide-capped Pd nanoparticles that were attributed to incomplete Pd^{2+} reduction, likely due to strong peptide-precursor interactions.[24, 39] The lack of Pd oxidation in the PdAu nanoparticles is likely attributed to shifts in the Pd^{2+} reduction potential due to the presence of nucleating Au clusters.

After background subtraction and edge-step normalization, the extended XAFS (EXAFS) data were converted to k-space and k^2-weighted (Figure S6), then Fourier transformed from 2.0-12.0 $Å^{-1}$ for the Au L_3-edge data and 2.0-10.0 $Å^{-1}$ for the Pd K-edge data as shown in Figure 2a-f. For the Pd foil standard, a main peak is positioned at 2.5 Å, which corresponds to the Pd-Pd nearest neighboring distance (Figure 2a-c). Note that due to photoelectron phase shift, this distance is lower than the observed Pd-Pd bond length of 2.75 Å found in fcc Pd. As such, the nearest neighbor distances observed in Figure 2a-f are similarly shifted. For Au L_3-edge comparisons, the split peak from the Au foil standard and subsequent nanoparticles stems from Townsend-Ramsauer resonance and represents the nearest neighbor Au-Au bond length. Due to the possibility of multiple overlapping scatterers in the bimetallic nanoparticles EXAFS data were modeled[40] (Figure S7-9) to obtain quantitative metal-metal bond lengths (Table 1). For monometallic Pd nanoparticles, Pd-Cl contributions were added due to the presences of unreduced Pd^{2+} as indicated from the Pd-XANES data (Figure S5) and previous observations on peptide-capped Pd nanoparticles.[39] Monometallic Pd nanoparticles exhibited Pd-Pd bond lengths of 2.74 ± 0.02 Å, 2.71 ± 0.01 Å, and 2.76 ± 0.02 Å for using AuBP1, H1, and Pd4 peptides respectively. Modeled Au-Au bond lengths of 2.88

± 0.01 Å, 2.87 ± 0.02 Å, and 2.84 ± 0.01 Å were obtained from AuBP1, H1 and Pd4 capped monometallic Au nanoparticles respectively. Note that differences in bond lengths from the bulk material are common in nanoscale materials due to stress and/or strain effects observed at the nanoscale.[38, 41]

For peptide-capped PdAu bimetallic nanoparticles, metallic bond lengths modeled from EXAFS provide insights into the local chemical environment on an element specific basis (Table 1). For example, Pd-Pd bond lengths closer to the bulk value of 2.75 Å would indicate a Pd fcc-like environment, while those with larger bond length would likely arise to structural conformation more akin to Au fcc. Conversely, Au-Au bond lengths closer to the bulk value of 2.88 Å would demonstrate local Au fcc-like structure, while a decrease would suggest a more Pd fcc-like structural arrangement. Similar observations and identifications can be made for modeled Pd-Au bond lengths as well. For PdAu nanoparticles capped with AuBP1, 3:1 and 1:1 PdAu demonstrate Pd metallic bond lengths that are more Pd fcc-like with modeled Pd-Pd and Pd-Au distances of 2.77 ± 0.02 Å and 2.80 ± 0.05 Å for 3:1 PdAu nanoparticles and 2.74 ± 0.02 Å and 2.79 ± 0.03 Å for 1:1 PdAu nanoparticles. Modeled Au-Au bond lengths for AuBP1-capped 3:1 and 1:1 PdAu are reduced from the bulk value (2.83 ± 0.01 Å and 2.83 ± 0.02 Å respectively), but are only slightly different from bulk Au. These findings suggest Pd atoms adopt a more Pd fcc-like structure, with slight shifts to larger nearest neighbor distances as indicated by the modeled Pd-Au distances, while Au atoms exhibit a more stained Au fcc-like structure. An increase in Au composition to 1:3 Pd:Au for AuBP1 capped nanoparticles further exhibits a shift to longer Pd-Au and Au-Au bond lengths (2.83 ± 0.03 Å and 2.85 ± 0.02 Å, respectively) indicating local Au structure is more similar to that of bulk Au, while the modeled Pd-Pd distance (2.78 ± 0.03 Å) is still more resemblant to bulk Pd. From these modeled bond lengths, Pd-Pd and Au-Au are only slightly affected by changes in composition and are more similar to their bulk values as opposed a weighted average value similar to the calculated Pd-Au bonds lengths, which would suggest a larger degree of phase separation over bimetallic alloying. Similar trends can be found from the modeled bond lengths from H1 and Pd4 capped PdAu bimetallic nanoparticles as shown in Table 1.

EXAFS modeling[40] (Figure S7-9) was also used to obtain element specific metal-metal CNs (Table 2), which are plotted vs. Pd composition Figure 2g-I, along with EXAFS Debye-Waller factors (Table S2). CNs specify the number of a particular metal type around a central data. For example, the Pd-Au CN is the average number of Au atoms around a Pd atom. Conversely, the Au-Pd CN is the average number of Pd atoms around a Au atom. For monometallic Pd nanoparticles, Pd-Pd CNs of 5.51 ± 2.65, 3.19 ± 0.8, and 4.95 ± 2.37 were obtained using AuBP1, H1, and Pd4, respectively. These CNs are significantly smaller than the expected theoretical value of 9.63 for spherical nanoparticles of this size.[42] This can be attributed to incomplete reduction of Pd^{2+} to Pd^{0}, as previously observed for peptide-capped Pd nanoparticles.[39] Conversely, monometallic Au nanoparticles have Au-Au CNs of 9.23 ± 0.72, 9.82 ± 1.17, 9.76 ± 0.72 for AuBP1, H1, and Pd4 respectively, which are similar to theoretical values.[42] For PdAu bimetallic nanoparticles, the calculated CNs are plotted as a function of Pd composition for each set of peptide-capped nanoparticles (Figure 2g-i). Note that for completely miscible bimetallic nanoparticles (100% random alloy), a linear trend in CN vs. composition is expected.[43] From the calculated CNs, each peptide has notable deviations from linearity, suggesting that the peptide at the biotic/abiotic interface is modulating nanoscale miscibility. For AuBP1 capped PdAu nanoparticles (Figure 2g), Au-Au CNs are higher than expected for a random alloy at 1:1 and 3:1 PdAu ratios, at 5.23 ± 1.28 and 7.00 ± 5.42 respectively. Additionally, the sum of Au-Pd and Au-Au CNs is greater than 8 for both these PdAu nanoparticles. Given that EXAFS is an ensemble-averaged technique, this would suggest a majority of Au atoms are surrounded by metallic atoms (i.e. not surface atoms), which would exhibit a CN of 12 for a fcc metal. For bimetallic nanoparticles synthesized with the H1 peptide, the calculated CNs further deviate from those expected for random alloys. All Pd-Pd CNs are comparative small (1.66 ± 1.36, 1.14 ± 1.03, and 1.52 ± 0.92 for 3:1, 1:1, and 1:3 Pd:Au nanoparticles respectively). Qualitatively, this would suggest minimal Pd-Pd interactions either through incorporation of Pd atoms in local Au environments, extensive Pd-Pd disorder, and/or Pd surface migration. Enriched Pd surface composition in 3:1 and 1:1 Pd:Au nanoparticles is further indicated by the relatively unchanged Au-Pd and Au-Au CNs with an increase in Pd composition from 1:1 to 3:1 (Table 2). Pd4-capped PdAu nanoparticles exhibit CN

trends that that deviate somewhat from linearity as well. The sum of Au-Au and Au-Pd CNs are approaching 9 or higher, which is close to the theoretical CN for monometallic nanoparticles of this size.[42] This suggests that the Au largely segregated into the core of the nanoparticles. It is important to note that the errors associated with CN calculations are largely contributed to the highly disordered nature of these nanoparticles,[44] as indicated by atomic PDF analysis and subsequent RMC modeling (see below). Taken together, the XAFS analysis clearly suggests PdAu phase separation in the peptide-capped PdAu nanoparticles which is influenced by the capping peptide.

While XAFS can provide detailed local structural information on bimetallic nanoparticle arrangements, structural information past the nearest neighbor coordination distances is challenging to obtain. The elucidation of atomic-scale structural information at larger distances is critical to assess sequence-dependent structure/function relationships, particularly for materials that may exhibit local variation in composition. As such, atomic PDF analysis of HE-XRD patterns was used to elucidate atomic-scale structural information over the length scale of the nanoparticles. Atomic PDFs are obtained via the Fourier transform of HE-XRD patterns, providing sub-Angstrom structural data in terms of atomic pair distances over comparatively large distances (> 20 Å).[45] Both Bragg and diffuse components of the HE-XRD pattern are considered, making this an optimal method to elucidate the atomic-scale structure of materials lacking long-range periodic order, such as nanomaterials.[24, 45] HE-XRD patterns (Figure S10) were taken on lyophilized powders using 115 keV irradiation, converted into total structure functions ($F(Q)$) (Figure S11) and Fourier transformed into atomic PDFs. Atomic pair distances are described in terms of relative atomic density in PDF analysis, where atomic PDF, $G(r) = 4\pi r[\rho(r) - \rho_0]$, exhibit peaks when the local atomic density ($\rho(r)$) is higher than the average atomic density (ρ_0). The PDFs oscillate to zero once the local and average atomic densities are equal, indicating the distance where long-range order is absent.

Figure 3 shows the atomic PDFs for all bimetallic nanoparticles capped with AuBP1, H1 and Pd4 up to 10 Å. Figure S12 & S13 present the atomic PDFs for both monometallic and bimetallic nanoparticles for comparison purposes, along with PDFs at 40 Å to illustrate the lack of long range structural order. In general, all atomic PDFs exhibited broadened features positioned in an fcc-type arrangement of atoms that

oscillates to zero at ~ 20 Å. The aforementioned features demonstrate the lack of structural order in the peptide-capped PdAu nanoparticles. Additionally, atomic PDFs exhibits peptide-dependent differences in relative peak intensity, peak broadening, and peak position at various length scales, signifying that nanoscale composition and structure is directly influenced by the capping peptide. For 3:1 PdAu nanoparticles, noticeable differences are observed in the first peak of the PDF, which originates from the first nearest neighbor distances in the bimetallic nanoparticles. For Pd4 capped PdAu at a 3:1 Pd:Au ratio, the first peak is centered 2.78 Å, which is slightly larger than the Pd-Pd nearest neighbor distance in bulk Pd of 2.75 Å This increase may be due to increased disorder in the bimetallic nanoparticles or an influence of Au incorporation. In 3:1 Pd:Au synthesized with H1, the first peak of the PDF is centered at 2.74 Å, with a notable shoulder at larger pair distances. This shoulder is likely attributed to atomic pair distances resembling a Au fcc lattice, which would indicate potential phase separation of Pd and Au. A similar first PDF peak is noted for AuBP1 capped 3:1 Pd:Au nanoparticles as well. At a 1:1 Pd:Au ratio, the first peak in the PDF for PdAu nanoparticles is located at a different average position for each peptide. For Pd4 capped PdAu at this ratio, a metallic nearest neighbor distance of 2.82 Å is observed, while a metallic nearest neighbor distance of 2.78 Å is observed for AuBP1 and H1 capped nanoparticles. These distances reflect an average metal-metal bond length somewhere between fcc Pd and fcc Au, and qualitatively suggests varying degrees of potential alloying or an ensemble average of bimodal populations of atoms that are either more Pd or Au-like. PdAu nanoparticles synthesized at a 1:3 Pd:Au ratio exhibit first PDF peaks positioned at a distance closely resembling a Au fcc structure, with AuBP1, H1, and Pd4 exhibiting peak locations at 2.82 Å, 2.80 Å, and 2.82 Å respectively. In addition, the lack of bimodal features in the region of the first metallic nearest neighbor distances suggests alloy nanoparticle homogeneity instead of significant populations of Pd-rich or Au-rich nanoparticles. Note that all reported bond lengths are consistent with EXAFS modeling (Table 1). Atomic PDF features at larger pair distances, which represent longer-ranger coordination spheres, exhibit changes in relative magnitude, peak shape and peak position, an indication that the capping peptide can directly influence bimetallic miscibility and structural coherency across length-scale of the nanoparticle. Overall, the

atomic PDFs clearly indicate atomic-scale structural differences that are certainly influenced by interactions with the capping peptide at the biotic/abiotic interface.

Atomic PDF analysis allows for structural modeling over the size of nanoparticles; however, directly quantifying local structure in terms of CNs cannot be obtained due to the lack of elemental specificity in traditional HE-XRD experiments. This presents a challenge when modeling atomic PDFs, as qualitative intuition may bias structural modeling efforts. Therefore, it is necessary to incorporate the CNs calculated from EXAFS modeling to guide atomic PDF structural analysis. To accomplish this, reverse Monte Carlo (RMC) simulations are used to model bimetallic and monometallic PDFs using the CNs generated from EXAFS modeling as a guide. RMC is an advantageous method for modeling materials lacking long range periodic order,[46, 47] including nanomaterials,[24, 25] as the method is not dependent on crystallographic constraints and is only guided by user inputted restrictions (see experimental section) and the experimental PDF data. In RMC, atoms in a starting configuration are moved at random and new atomic PDFs are calculated after each move. Atomic moves are accepted or rejected based on the Metropolis criterion,[48] and is repeated until the RMC generated PDF converges to the experimental PDF. As shown in Figure 3 (red lines), RMC generated PDF fit the experimental data reasonably well, with agreement factors (R_w) all below 15%, providing experimentally accurate nanoparticle configurations.

PdAu nanoparticle configurations generated by RMC modeling of the experimental PDF data and guided by EXAFS modeling results are shown in Figure 4 (see Figure S14, for RMC cross sections). Each nanoparticle exhibits disordered surfaces with surface compositions varying with differences in capping peptide. For PdAu nanoparticles at a 3:1 Pd:Au ratio, a strong preference for surface Pd is clearly observed (Figure 4a-c). AuBP1 capped 3:1 Pd:Au nanoparticles exhibit a larger fraction of surface Au atoms (Figure 4a), while H1 and Pd4 (Figure 4b&c) adapt more of a core-shell type of arrangement. An analysis of surface atoms for these configurations reflect these observations, wherein 89.0% of surface atoms in AuBP1 capped PdAu nanoparticles are Pd, while 92.2 and 100% are observed for Pd4 and H1 respectively at a 3:1 Pd:Au composition. For nanoparticles synthesized at a 1:1 Pd:Au ratio (Figure 4d-f), RMC generated configurations still exhibit Pd surface segregation, which is dependent on the

capping peptide. For AuBP1 and H1 capped configurations (Figure 4d&e), 66.4% and 67.4% of surface atoms are Pd, while in Pd4 (Figure 4f) the surface of Pd atoms increases to 73.8%. For PdAu nanoparticles synthesized at a 1:3 Pd:Au ratio, nanoparticle configurations still exhibit some enrichment of Pd, wherein 36.3% of all surface atoms are Pd for AuBP1 and H1 capped samples, and 42.0% surface atoms are Pd in PdAu capped with Pd4. In previous work of PdAu nanomaterials synthesized within the R5 peptide template, which has no known specificity toward Pd or Au, random alloys of PdAu were obtained across all tested compositions.[26] This indicates that deviations from random alloyed structures are not simply induced by common peptide functionality (amide bonds, hydrogen bonding moieties, etc.), but more likely through complex interactions at the biotic/abiotic interface that are sensitive to the primary sequence of the peptide.

To examine the influence of the peptide sequence at the biotic-abiotic interface, atomic PDFs were calculated from the surface layers of atoms of the RMC-generated configurations (Figure S15, see Experimental Section for details). For AuBP1-capped 3:1 Pd:Au nanoparticles, a calculated metallic nearest neighbor distance is located at 2.72 Å, which is a shorter distance than observed over the entirety of the nanoparticle. H1-capped PdAu nanoparticle at this ratio display a calculated nearest neighbor distance of 2.76 Å, while 3:1 Pd:Au Pd4-capped nanoparticles exhibit a much larger comparative distance at 2.90 Å. More interestingly, an even shorter feature for H1 and Pd4-capped 3:1 PdAu nanoparticle are observed at 2.38 Å for each nanoparticle. While profound, extensive surface contraction of metallic nearest-neighbor distances has been reported previously.[49-51] In this instance, H1 and Pd4 binding likely influence surface disorder in a similar fashion, probably through the common amino acids at the N-terminus half of each peptide. It is worth noting that the entropic nature of RMC may overestimate the surface bond length contraction,[24] but would do so evenly across all comparable calculations such as those in this paper and is thus still valid for comparative purposes. For 1:1 Pd:Au nanoparticles, the main surface nearest neighbor distance are calculated at 2.72 Å, 2.77 Å, and 2.70 Å for AuBP1, H1, and Pd4-capped nanoparticles respectively, again smaller than anticipated based on bulk values and those found in PDFs in Figure 3. The smaller distances observed in H1 and Pd4-capped 3:1 Pd:Au nanoparticles are less pronounced,

appearing as shoulders to the main feature positioned at 2.40 Å and 2.47 Å respectively. Increasing the Au content to 1:3 Pd:Au, all peptide-capped PdAu have a calculated surface nearest neighbor distance at 2.76 Å, while H1 and Pd4-capped nanoparticles exhibit much shorter features at 2.36 Å, akin to the observations in the 3:1 Pd:Au nanoparticles. Overall, this analysis suggests that peptides have multi-functionality; not only can the biotic/abiotic interface be used to tune composition, but also the local atomic disorder at the surface.

Next, REST-MD simulations were performed to gain insights into how the conformations of the adsorbed peptides may differ on the two zerovalent monometallic interfaces, therefore potentially offering insights into how these peptides influence the segregation of the metals in the nanoparticles. Note that in general we expect that there is no single 'adsorbed configuration' can describe the surface-adsorbed state for these types of materials-binding sequences, which are thought to be intrinsically disordered.[25] Standard MD simulations cannot deliver adequate conformational sampling to capture this phenomenon[37] and may give rise to misleading conclusions. Currently, there are few reports in the literature regarding molecular simulations of non-covalent peptide interactions at aqueous noble metal bimetallic interfaces. Heinz *et al.* reported simulations of a number of peptide sequences adsorbed at a stripe-morphology aqueous Pd/Au interface.[33] Though fundamentally informative, the sharp interface between the Au and Pd stripes used in that study does not resemble the alloyed or core-shell structures observed in the PdAu nanoparticles described in the current study.

One of the major reasons for the lack of published simulation data regarding adsorption of peptides at bimetallic aqueous interfaces is the complete lack of reliable FFs to describe the interaction of biomolecules at aqueous bimetallic interfaces consisting of random or layered (mimicking core-shell) arrangements of atoms. This is in stark contrast with the case for monometallic/peptide force-fields, which are relatively more mature in terms of development and validation.[31, 52-54] We emphasize that merely mixing the known force-field parameters for Au and Pd surfaces, without extensive testing and validation steps, will likely produce incorrect and misleading data for peptide adsorption. Therefore, as a conservative measure and as a prelude to substantial future efforts to construct and test such FFs, we used REST-MD simulations to model each of the three

peptides adsorbed at either of the two monometallic aqueous interfaces, Au(111) and Pd(111). In our previously published study, we showed that the binding modes of peptides adsorbed at the aqueous planar Au interface shared a strong degree of similarity with the corresponding binding modes at the aqueous Au nanoparticle interface, as quantified by several metrics.[25] Therefore, it is highly likely that our current REST-MD simulations of peptides adsorbed at the aqueous Au/Pd(111) interfaces are reflective of the both the principal contact modes (*i.e.* the number, location and type of "strong binding" residues) and the conformational entropic contributions of these same peptide sequences adsorbed at the corresponding aqueous nanoparticle interface.

Our objective with these simulations was to predict and quantify the differences between the adsorbed conformational ensembles of the peptides, and to investigate the connections between these data and the sequence-dependent enrichment phenomena observed in experiment. As our findings summarized herein demonstrate, the surface adsorption characteristics of each of the three peptide sequences at the aqueous Au(111) interface was found to be very similar to that at the aqueous Pd(111) interface. This suggests that the peptide-surface binding motif for each of the three peptides will broadly share a high degree of similarity over all Pd:Au ratios.

Figure 5 shows the degree of direct contact that each residue had with the metal surface for each of the three peptides, calculated from our REST-MD simulation trajectories (percentage values are provided in Table S3). These data demonstrate that the general contact pattern for each of the three peptides is very similar across the two different metal surfaces. AuBP1 had seven and eight residues that are in direct contact with the Au(111) and Pd(111) interfaces respectively for more than 75% of the REST trajectories. Herein, we denote such residues as "anchor" residues. Moreover, these anchor residues were distributed throughout the length of the AuBP1 sequence (Figure 5). In contrast, Pd4 has on average only two anchor residues, located near each of the chain ends. In the case of H1, the contact pattern appears to be a blend of the contact characteristics of the two parent peptides, with six and five residues acting as anchors on Au(111) and Pd(111), respectively. In previous simulation studies regarding the adsorption of peptides at the aqueous Au(111) interface,[25] it was possible to generate a measure of the degree to which enthalpic contributions played a role in peptide-surface

binding by first identifying which residues were anchors, and subsequently combining this information with the energy of adsorption of the amino-acid corresponding to each anchor residue. However, we cannot apply such an analysis to the Pd(111) system, because the adsorption energies of amino-acids to the Pd(111) interface have not been reported to date. Because of this limitation, here we instead used the number of anchor residues as a qualitative measure of relative enthalpic contributions to peptide-surface adsorption, with these data indicating a trend in binding strength of AuBP1 > H1 > Pd4. Representative snapshots of the peptides adsorbed at the aqueous metallic interfaces, highlighting the contact between the surface and the anchor residues (such as Arg, Trp and His), are provided in Figure S16 of the Supporting Information. These images, along with histograms (generated from the entire REST-MD trajectories) of the orientation of the plane of the rings, or in the case of Arg, the guanidinium group, indicate that in most instances these groups were, on average, oriented approximately flat on the Au surface (see Figure S17, Supporting Information).

The number and relative population of distinct conformations of the peptide in the surface-adsorbed state are factors in determining the binding strength of a peptide for a given material.[37] For instance, a greater number of distinct surface-adsorbed conformations of a peptide means that there are a greater number of basins on the potential energy landscape corresponding with this adsorbed system. This in turn can contribute to a stronger peptide-material affinity. Each distinct conformation can be obtained from a clustering analysis, whereby "like structures" can be grouped together (see the Supporting Information and previous studies[25, 34, 37, 53] for more details on this procedure). Herein we refer to each "like structure" as a "cluster". As detailed in earlier studies, the conformational entropic contribution of the adsorbed peptides, S_{conf}, can be calculated from:

$$S_{\mathrm{conf}} = \sum_{i=1}^{n} - p_i \ln(p_i)$$

where p_i is the relative population of each cluster and n is the total number of clusters, as determined for each REST-MD trajectory. This conformational entropic contribution to the binding of the peptides on the two different surfaces is given in Table 3, and the

relative populations of the top-ten most populated clusters is provided in Table S4. As found with the residue-surface contact data, the three peptide sequences show very similar trends across the two surfaces. Specifically, differences in S_{conf} between the two metals were less than 0.1. However, the values of S_{conf} for the three peptides adsorbed on each metal surface are distinctly different. The number of clusters was greatest for Pd4, followed by H1, with AuBP1 having the least number of clusters.

These results are in agreement with findings from previously-published simulations of AuBP1 and Pd4 adsorbed at the aqueous Au(111) interface[37] generated using the GolP-CHARMM FF,[53] where it was found that AuBP1 was a primarily an enthalpically-driven binder (*i.e.* AuBP1 supported a relatively smaller number of adsorbed conformations, with each conformation making strong contact with the Au surface through a relatively high proportion of anchor residues). These studies also found Pd4 to be an entropically-driven binder; this sequence featured a large number of adsorbed conformations, where each conformation has relatively fewer anchor residues. Our predictions of the intrinsically-disordered traits of the conformational ensemble for these peptides adsorbed when at the aqueous Au interface agree with previously-reported circular dichroism (CD) spectroscopy data.[21] While further structural information, such as from nuclear magnetic resonance, Raman, or Fourier-transform infrared spectroscopies, would be valuable, the random-coil character of these peptides in the adsorbed state renders this an extremely challenging task in itself.[55-57]

Our results in the present study show that this characterization is also true for the aqueous Pd(111) interface. Again, the hybrid sequence H1 displays characteristics between those of the two parent peptides. By comparing the trend in the conformational entropic contribution to adsorption with the degree of Pd surface segregation seen in the AuPd nanoparticles for each peptide, we note that the order is the same (Pd4 > H1 > AuBP1), and is the inverse of that observed for the enthalpic contribution, namely the number of anchor residues. Thus, on the basis of the peptides sequences tested here, our findings indicate that use of entropically-driven peptide sequences might facilitate the generation of core-shell AuPd particles peptides. Encouragingly, the somewhat subtle differences observed via the PDF functions for the enrichment of Pd atoms on the bimetallic nanoparticle surface are reflected by similar differences seen for the adsorption

modes of our three peptides on the Au and Pd surfaces. Future efforts will be directed at developing genuine peptide/bimetallic force-fields, which can be used to predict the structure of the bimetallic-nanoparticle/peptide aqueous interface. In principle these structures could be used as a basis for first-principles calculations of the electrocatalytic properties of these systems and thus make conceptual links between the peptide sequence and the resulting electrocatalytic response. However, in practice this goal remains elusive, due to the ongoing challenges in fully realizing a first-principles electrochemical approach.[58]

The highly disordered nanoparticle surfaces and Pd surface segregation observed in the peptide-capped PdAu nanoparticles suggests that peptides could be used to potentially tune surface disorder[24, 25] and surface composition. Two significant driving forces behind bimetallic miscibility are cohesive energy and surface energy.[7] In this context, Au is expected to surface segregate in a PdAu bimetallic system. Pd exhibits a higher cohesive energy than Au (376 kJ/mol vs. 368 kJ/mol),[59] thus providing a driving force for Pd to be highly coordinated with other metallic atoms. The surface energy of Au is lower than Pd as well (1.50 J/m^2 vs. 2.05 J/m^2),[60] which should further induce Au surface segregation. Along these lines, previously reported computational segregation energies from 55 atom nanoparticles suggest Au surface segregation in a PdAu system,[61] despite bimetallic nanoparticles of this size commonly resulting in alloyed materials to due to lack of metal atom diffusion length.[7] The Pd surface biasing observed in the peptide-capped Pd nanoparticles is thus heavily influenced by the interactions between the peptide and the bimetallic nanoparticles. Pd surface segregation has been observed previously using traditional one-pot nanoparticle synthesis chemistries,[62, 63] which is likely driven by surface interactions occurring during nanoparticle synthesis. Note that interactions between the peptides and precursors may affect metal reduction and bimetallic miscibility,[5, 24, 64-67] and will be the subject of future study to obtain a more complete understanding between synthesis, the driving forces behind bimetallic miscibility, and bimetallic/biotic surface interactions. Nevertheless, the lack of modularity and complexity of commonly employed surface ligands limits surface segregation engineering, wherein peptides may provide a means to rationally design bimetallic nanoparticle surfaces.

To evaluate the catalytic properties of the peptide-enabled PdAu nanoparticles, electrocatalytic methanol oxidation experiments were performed under alkaline conditions using cyclic voltammetry (CV). This testbed reaction is the anodic component in direct methanol fuel cells (DMFCs),[68] wherein improved understanding and performance of alkaline electrochemical methanol oxidation could help progress the maturation of this technology. For monometallic Pd nanoparticles (Figure S18a), peaks corresponding to the oxidation of methanol[69, 70] appear at -90 mV vs. Hg/HgO for AuBP1 and Pd4-capped nanoparticles on the forward scan, while H1-capped nanoparticles are completely inactive. Pd4-capped Pd nanoparticle exhibit a four-fold increase in current output as compared to AuBP1-capped Pd nanoparticles, indicating the capping peptide can have a drastic influence on catalytic properties. On the reverse scan, a prominent feature is observed at -300 mV vs. Hg/HgO for AuBP1 and Pd corresponding to the removal of surface absorbed CO which originates from the initial methanol oxidation in the forward scan (Figure S18a). Note that a small peak is observed in H1-capped Pd nanoparticles at -195 mV vs. Hg/HgO, suggesting a small amount of absorbed material at the Pd surface is being removed in the reverse scan. In the same scan range, very little methanol oxidation is observed for monometallic Au nanoparticles (Figure S18b). These results are anticipated, as Au is known to have lower alcohol oxidation activity as compared to Pd.[71, 72] In addition, Au catalyzed methanol oxidation occurs at higher potentials than Pd.[73]

Electrochemical methanol oxidation results for peptide-capped PdAu nanoparticles are shown in Figure 6. At 3:1 Pd:Au, Pd4-capped exhibit substantially improved methanol oxidation capability compared to Pd4-capped Pd nanoparticles (6 and S18). Interestingly, bimetallic nanoparticles capped with either AuBP1 or H1 exhibit minimal methanol oxidation (Figure 6a). This finding suggests the surface structure of the PdAu nanoparticles capped with Pd4 maintains a more ideal catalytic surface properties for methanol oxidation as compared to those capped with H1 or AuBP1 during electrochemical oxidation. For bimetallic nanoparticles made at 1:1 Pd:Au, both Pd4 and AuBP1 capped nanoparticles exhibit moderate methanol oxidation, where H1 is again catalytically inactive (Figure 6b). A shift in potential is noted for 1:1 Pd:Au nanoparticles, which now have a maximum methanol oxidation potential at -40 mV and -

35 mV vs. Hg/HgO for Pd4 and AuBP1-capped nanoparticles respectively. This shift in potential is likely due to the increased amount of Au at the nanoparticle surface, which oxidized methanol at higher potentials.[73] Such shifts in potential at maximum methanol oxidation have been previously observed in other PdAu nanoparticle systems.[74, 75] Interestingly, there is also an increase in absorbant removal compared to methanol oxidation at a 1:1 Pd:Au vs. 3:1 Pd:Au. For 1:3 Pd:Au, AuBP1 and Pd-capped exhibit an onset of methanol oxidation at ~-100 mV vs. Hg/HgO, while H1-capped nanoparticeles are again inactive (Figure 6c). The increase in current does not decrease due to CO poisoning and continues into oxygen evolution potential window. For comparison purposes, electrochemical methanol oxidation experiments were performed on commercially available Pd/C. Catalyst inks were prepared in an analogous fashion to the peptide-capped bimetallic nanoparticles. Surprisingly, minimal methanol oxidation was observed in the background corrected CV (Figure S19) at comparable potentials to the PdAu bimetallics, however; an anodic peak starts at ~400 mV vs Hg/HgO. Though unknown at this time, we hypothesize that the increase in current is likely combination of Pd surface oxidation[76] and possibly methanol oxidation, although the latter is more unlikely given the recorded potential. The lack of methanol oxidation would suggest the quaternary amine ionomer is blocking catalytic sites on the bare Pd/C control, and furthermore, indicates that the peptides are likely still bound to the nanoparticle catalysts and thus influencing electrocatalytic methanol oxidation.

The electrochemical methanol oxidation results indicate that catalytic activity is highly dependent on the capping peptide, which influences structural and chemical properties at the nanoparticle surface both after synthesis (see above) and likely during electrocatalysis. Put into context, recent work by Brodsky *et al.* illustrates that ~30 nm core-shell Au@Pd with 1.5 nm Pd shell thickness maintains maximum activity activity for electrochemical ethanol oxidation under alkaline conditions until Au atoms begin to migrate to the surface.[73] This was attributed to competing lattice strain and electronic effects, wherein lattice strain increases Pd adsorbate bonding strength while electronic effects results in d-orbital electron density decreases in Pd, which decreased adsorbate bonding in Pd.[73, 77] Maximum catalytic activity is likely achieved at an optimal PdAu surface composition/structure, where adsorbate bonding is neither too high to prevent

catalytic turnovers nor too low to initiate catalysis. In the peptide-capped bimetallic nanoparticles, an increase in Pd:Au ratio is noted at the surface compared to the bulk, particularly for Pd4 and H1 capped nanoparticles. Changes to the surface composition likely occur depending on the nature of the peptide at the biotic/abiotic interface, and may be more pronouced than those observed by Brodsky *et al*.[73] given that our particle size is much smaller (~ 2 nm vs. ~ 30 nm). As such, we attribute increases in catalytic activity found in Pd4, and to a lesser extend, AuBP1-capped nanoparticles to the capping peptides ability to effectively resist an undesirable amount of Au surface migration that would reduce catalytic activity. In addtion, the capping peptide orientation on the nanoparticle surface may additionally prevent methanol oxidation by blocking highly catalytic sites. Substantial changes in catalyic activity with repeated cycling were not observed, and thus we expect the capping-peptide is still present during methanol oxidation experimentation. While surface ligand removal is commonly observed in many metallic and bimetallic nanoparticle systems during CV experiments, typical surface ligands are not material specific. Peptides, on the only hand, have an inherently high affinity for material surfaces as they are discovered via biocombinatorial process, often selected out of 10^9 potential binding ligands. Taking these considerations into account, it is clear that the capping peptide has a profound effect on the catalytic activity for nanoparticles with identical bimetallic composition. Understanding structural changes during electrocatalysts using in-situ XAFS and HE-XRD would provide additional insights to sequence-dependent catalytic activities, and is the subject of future reports.

Conclusions

In summary, PdAu bimetallic nanoparticles were synthesized using known Pd and Au binding peptides, along with a hybrid sequence exhibiting established binding motifs for both Pd and Au. The resulting nanoparticles were ~ 2 nm in size at all bimetallic ratios and indicate a surface enrichment of Pd, likely attributed to strong Pd-peptide interactions dependent on peptide sequence. The catalytic properties of the nanoparticles were evaluated for electrochemical methanol oxidation under alkaline conditions, wherein catalytic activity is clearly influenced by the capping-peptide for materials with identical bimetallic composition. Our findings demonstrate the promising capability of peptides to influence bimetallic surface composition and structure, potentially providing a

means to rationally design peptide-enabled bimetallic nanoparticles. A more comprehensive elucidation of the sequent-dependent structure/function relationships of these systems will be needed in the future to realize this goal.

Experimental

Nanoparticle synthesis. PdAu nanoparticles were synthesized using an adapted procedure for peptide-capped Au nanoparticles.[21] Briefly, 500 μL of a 1.0 mM solution of peptide was added to 4.46 mL of water. All three peptides (AuBP1, H1 and Pd4; see Table 1) were purchased from Peptide 2.0 at 95% purity. A total of 10 μL of 0.1 M of K_2PdCl_4 and/or $HAuCl_4$ (Sigma Aldrich) to was added to this solution to the desired Pd:Au ratio. For example, the synthesis of 3:1 Pd:Au nanoparticles used 7.5 μL of 0.1 M K_2PdCl_4 and 2.5 μL of 0.1 M $HAuCl_4$. This solution was stirred for at least 10 min, followed by the addition of 30.0 μL of freshly prepared 0.1 M $NaBH_4$ to reduce the metal salts to zerovalent alloyed nanoparticles. The reduction reaction was allowed to proceed unperturbed for at least 1 h prior to characterization or catalytic testing. Double distilled, 18.2 MΩ•cm water was used in all experiments.

Characterization. Scanning transmission electron microscopy (STEM) imaging for sizing analysis was performed on a spherical aberration corrected JEOL-ARM 200F operating at an accelerating voltage of 200 kV. The microscope was operated in scanning mode, all images shown are annular dark field (ADF) STEM images. The detector inner collection angle for HAADF imaging was ≈ 70 mrad; high resolution imaging was performed with a spot size of 8c and pixel dwell time of 25 μs. Samples were prepared on ultrathin carbon TEM grids (Ted Pella, USA) by drop casting 5 μL of nanoparticles diluted by a factor of 50 onto the grid and drying them in air. Prior to high resolution imaging the samples were cleaned for 45 seconds in a 97% H_2, 3% O_2 plasma to remove hydrocarbon contaminants (Fischione model 1070). Mean particle sizes for each unique Pd:Au ratio and peptide were determined from size measurements of at least 200 nanoparticles from 5 randomly selected areas on the sample. Nanoparticle sizes were measured using custom automated image analysis MATLAB algorithms, with particle size distributions normalized to the total integral to yield a probability density function. STEM Energy dispersive x-ray spectroscopy (STEM-EDS) elemental mapping was

performed on a FEI Talos F200X operating at 200 kV equipped with a Bruker ChemiSTEM EDS system. Pixel intensities in the EDS maps for gold and palladium were computed by integrating the $L\alpha_1$ peaks of each element.

XAFS was performed at the 12-BM beamline, Advanced Photon Source, Argonne National Laboratory using a water-cooled, double crystal, fixed-exit monochromator with Si(111) crystals. Lyophilized powders were spread across Kapton tape for analysis at both the Pd K-edge (24.35 keV) and Au L_3-edge (11.92 keV) at 200 eV before to 900 eV after each respective adsorption edge using a 13 channel Ge detector. The raw data was processed using the Athena program and modeled with FEFF6 theory[78] using the Artemis program from the IFEFFIT XAFS analysis software.[40] Standard foils of Pd and Au were first modeled to obtain S_0^2 values of 0.835 and 0.868 for Pd and Au, respectively. Subsequent modeling of nanoparticles was performed exclusively using metal-metal contributions, with the exception of monometallic Pd nanoparticles, which required Pd-Cl contributions for satisfactory modeling. Bimetallic nanoparticles models were performed by simultaneously fitting both Au L_3-edge and Pd K-edge data using Pd fcc, "Au-doped" Pd fcc, "Pd doped" Au fcc, and Au fcc theoretical paths.

HE-XRD patterns we obtained at the 11-ID-C beamline of the Advanced Photon Source, Argonne National Laboratory using 115 keV irradiation. Lyophilized nanoparticle samples were loaded into 1.0 mm diameter Kapton capillaries and diffracted X-ray intensities were collected by a large area detector. HE-XRD patterns were background scattering corrected, converted into F(Q), and Fourier transformed into PDFs using the program RAD.[79]

RMC Modeling. To obtain nanostructure configurations, atomic PDF data was modeled with reverse Monte Carlo (RMC) simulations using RMC++,[80] wherein the coordination numbers (CNs) obtained from EXAFS modeling were used to guide the RMC simulations of the atomic PDF data. Spherical truncates of ideal crystals served as starting configurations for RMC simulations which reflected the average nanoparticle size obtained from TEM sizing analysis. Spherical models serve as good approximations to the elongated morphologies observed from TEM.[26, 81, 82] Each starting configuration consisted of a random distribution of Pd and Au atoms. For materials with a Pd composition >50%, a Pd lattice was used as starting structure, while a Au lattice was used

for all other samples. Constraints in the RMC simulations included minimum metal-metal bond length distances and CNs generated from EXAFS modeling. To ensure CN constraints were met and to remove any possible local configuration biasing from the starting configurations, 10% of the RMC moves allowed for two atoms to swap positions. Analysis of the bimetallic nanoparticle surface structure was done by calculating atomic PDFs of the surface atoms (~ 0.5 nm from the surface) of the RMC-generated configurations using the program I.S.A.A.C.S.[83]

Replica Exchange with Solute Tempering (REST) Molecular Dynamics Simulations. REST-MD simulations of each of the three peptide sequences (Pd4, AuBP1 and H1, see Table 1) adsorbed at either the aqueous Au(111) interface or the aqueous Pd(111) interface were performed. Three-dimensional periodic boundary conditions were used throughout. Each system comprised a single peptide chain, a metallic slab (presenting either the Au(111) or Pd(111) facet) constructed as a $p(20\times24)$ supercell, with a slab thickness of five atomic layers. During the simulations the metal atoms were free to move. A total of 6605 water molecules were added to the inter-slab space perpendicular to the slab surface, and the length of the simulation cell was adjusted along this direction to ensure that liquid water in the center of the inter-slab space exhibited the bulk water density corresponding to room temperature and 1 atm of pressure. An appropriate number of Cl^- counter-ions were added to the solvent to ensure overall charge neutrality of the simulation cell. All REST-MD simulations were performed using the GROMACS v5.0 software package.[84]

The CHARM22* force-field (FF)[85, 86] was used to described the peptides, with water molecules modeled using the modified version of TIP3P[87, 88] compatible for the CHARMM FFs. A modified version[25] of the CHARMM-METAL FF[52] was used to describe the inter-atomic interactions involving the Au atoms. In general, in molecular simulation a compromise must be made between the level of detail at which the interatomic interactions are described and the time-scales and length-scales that can be feasibly captured in that simulation. As mentioned earlier, the intrinsically-disordered character of these peptides presents a significant challenge in terms of satisfying a high degree of conformational sampling using molecular simulations. The time-scales and length-scales required for this thorough sampling of this interfacial conformational

ensemble renders a quantum mechanical approach impractical. To this end, we have modeled the interatomic interactions using well-established force fields.[25] The simulations were performed in the canonical (*NVT*) ensemble using 16 replicas, spanning an "effective temperature" window of 300-500 K. Additional information on the simulations details, the contact residue analysis and cluster analysis is provided in Section S3 "Simulation Details", in the Supporting Information.

Electrocatalysis. All peptide-capped nanoparticle samples were evaluated for electrocatalytic methanol oxidation under alkaline conditions using cyclic voltammetry (CV). A three-electrode configuration consisting of a Hg/HgO reference electrode, graphite counter electrode, and nanoparticles deposited on glassy carbon electrodes was used for all CV experiments. A total of 4.0 μL of nanoparticle inks were dropcast onto glassy carbon for each experiment. Nanoparticle inks were prepared by first sonicating ~1 mg of acid-cleaned Vulcan XC-72 carbon (Cabot Corporation) in 350 μL of isopropyl alcohol, followed by the addition of 600 μL of as synthesized nanoparticles and 50 μL of a quaternary ammonium-based random copolymer (at 5 mg/mL in methanol) as an ionomer. See the Supporting Information for the synthesis and characterization details of the ionomer.[89, 90] CV experiments were ran from -0.7 V to 0.3 V vs. Hg/HgO starting at open-circuit voltage of the half cell. Nanoparticles were first cycled in 1 M NaOH to obtain a constant background CV, followed by the addition of 1 M methanol for electrocatalytic oxidation experiments. CV results were normalized to the mass of Pd in the nanoparticles given its reported superior alcohol oxidation properties as compared to Au.[91, 92] For comparison purposes Pd/C (Sigma) was investigated using identical preparation.

Supporting Information

The Supporting Information is available free of charge on the ACS Publications website at DOI: 10.1021/acsnano.XXXXXXX, which includes synthesis details of the ionomer used in this study, REST-MD simulation details and corresponding results, HR-TEM images of all nanoparticles used in this study, raw data from all synchrotron radiation experimentation, cross sections of RMC-generation bimetallic nanoparticles, and electrocatalytic data from peptide-capped monometallic nanoparticles.

Author Information

*Email: nicholas.bedford@nist.gov

Acknowledgments

The use of beamlines 11-ID-C and 12-BM of the Advanced Photon Source is supported by the U.S. Department of Energy (DOE) Office of Science User Facility operated for the DOE Office of Science by Argonne National Laboratory under Contract No. DE-AC02-06CH11357. ZEH thanks the Royal Society of Chemistry (RSC) for travel funds made available under the Journal Grants for International Authors scheme to assist in facilitating the reported research. This research was undertaken with the assistance of resources from the National Computational Infrastructure (NCI), which is supported by the Australian Government. TRW thanks **veski** for an Innovation Fellowship. This work was partially supported by the Air Force Office for Scientific Research (TRW, Grant No. FA9550-12-620 1-0226). The SPE and EBC gratefully acknowledge financial support from the Army Research Office through a MURI award, W911NF-10-1-0520, and the central analytical facilities supported by the NSF-Sponsored MRSEC at UMass Amherst. We would like to thank Prof. Brian Gorman of the Colorado School of Mines with assistance with EDS mapping experiments.

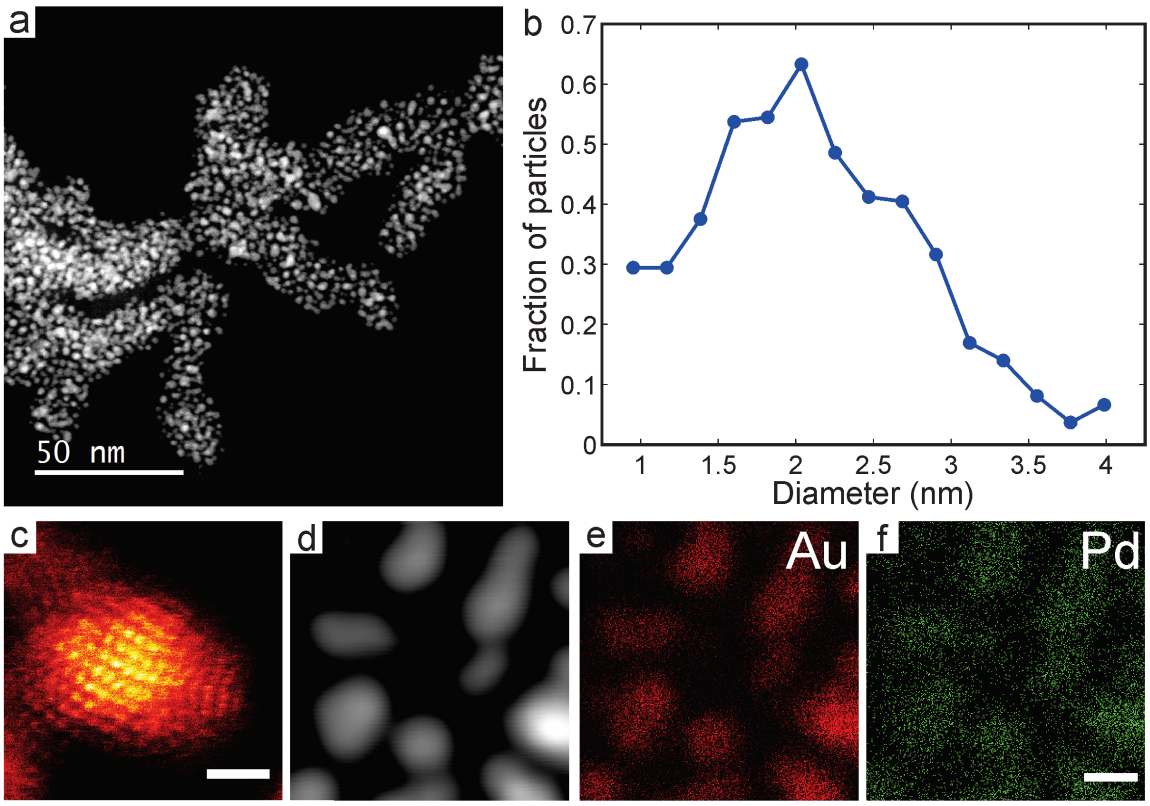

Figure 1. STEM imaging and elemental mapping of AuBP1-capped 1:3 Pd:Au nanoparticles: a) Representative low magnification HAADF-STEM image used for particle size determination; b) particle size distribution; c) false colored atomic resolution image of a single nanoparticle (Scale bar is 1 nm); d) HAADF-STEM image of several nanoparticles used for subsequent EDS mapping; e) Au STEM-EDS map; f) Pd STEM-EDS map (Scale bar is 2 nm).

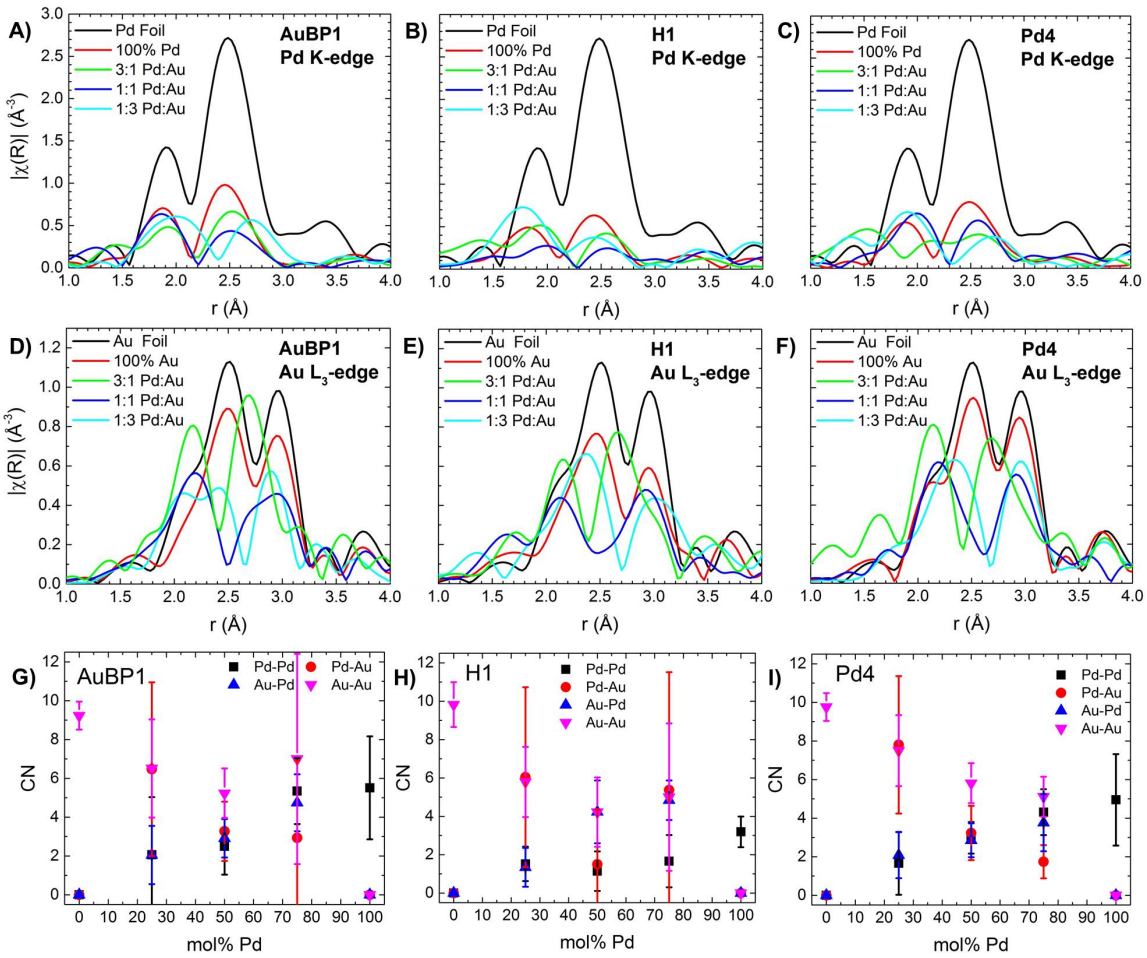

Figure 2. Pd-EXAFS for a) AuBP1, b) H1, and c) Pd4 capped bimetallic and monometallic nanoparticles; Au-EXAFS for d) AuBP1, e) H1, and f) Pd4 capped bimetallic and monometallic nanoparticles and; resulting CNs from EXAFS modeling at both the Pd K-edge and Au L_3-edge simultaneously.

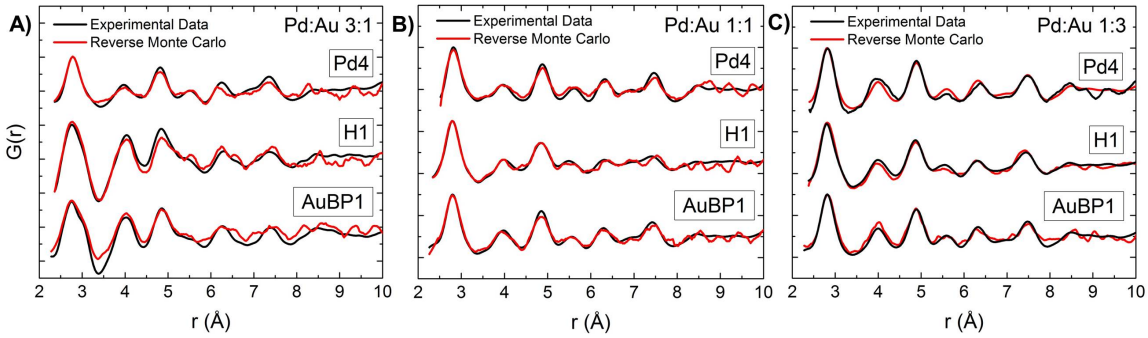

Figure 3. Atomic PDFs (black lines) and corresponding RMC fits (red lines) for peptide-capped bimetallic PdAu nanoparticles at a) 3:1 PdAu; b) 1:1 Pd:Au; c) 1:3 Pd:Au. PDFs offset for clarity.

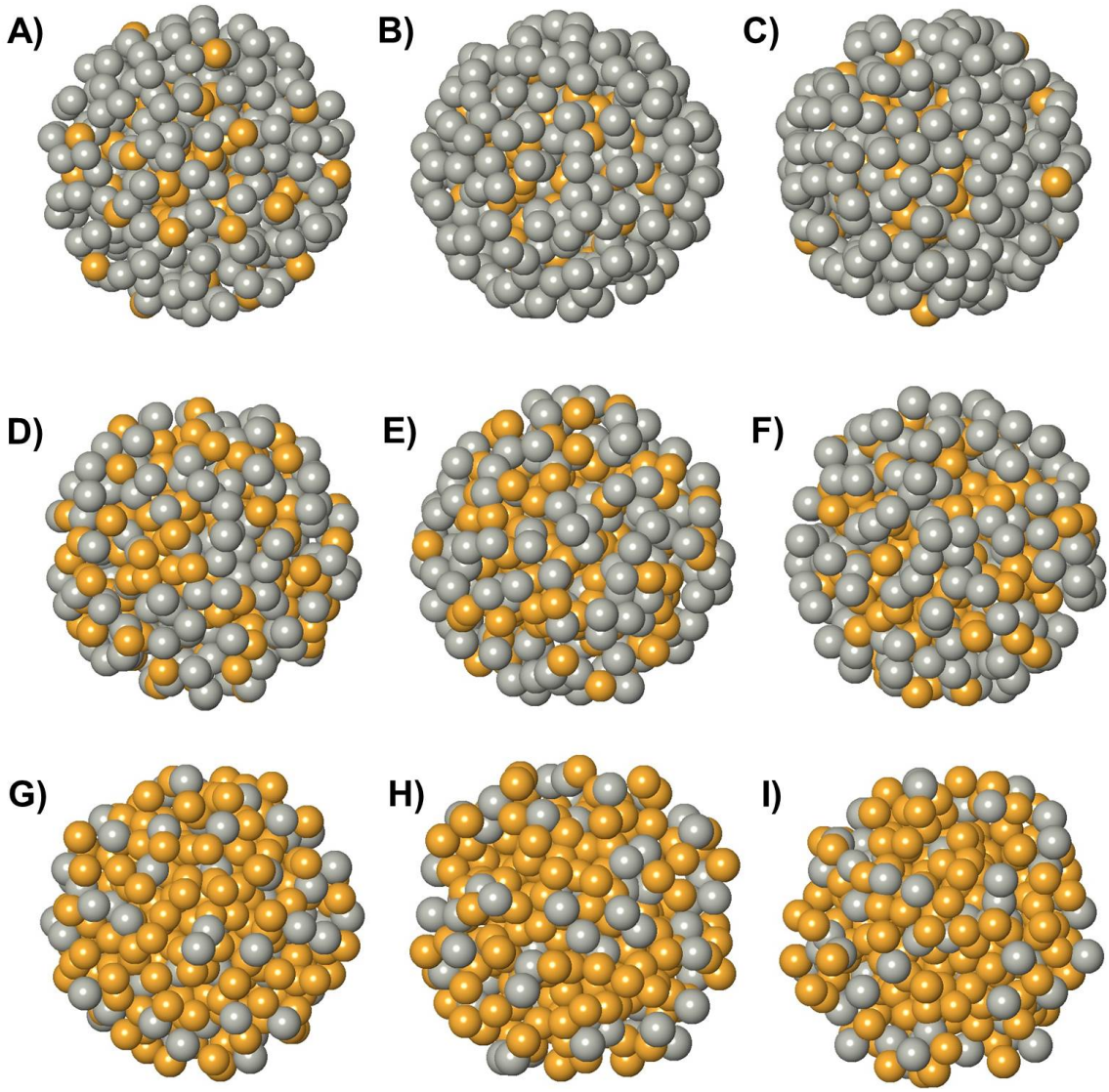

Figure 4. Model bimetallic nanoparticle configurations generated from RMC simulations of atomic PDFs for a) AuBP1 3:1 Pd:Au; b) H1 3:1 Pd:Au; c) Pd4 3:1 Pd:Au; d) AuBP1 1:1 Pd:Au; e) H1 1:1 Pd:Au; f) Pd4 1:1 Pd:Au; g) AuBP1 1:3 Pd:Au; h) H1 1:3 Pd:Au; and i) Pd4 1:3 Pd:Au.

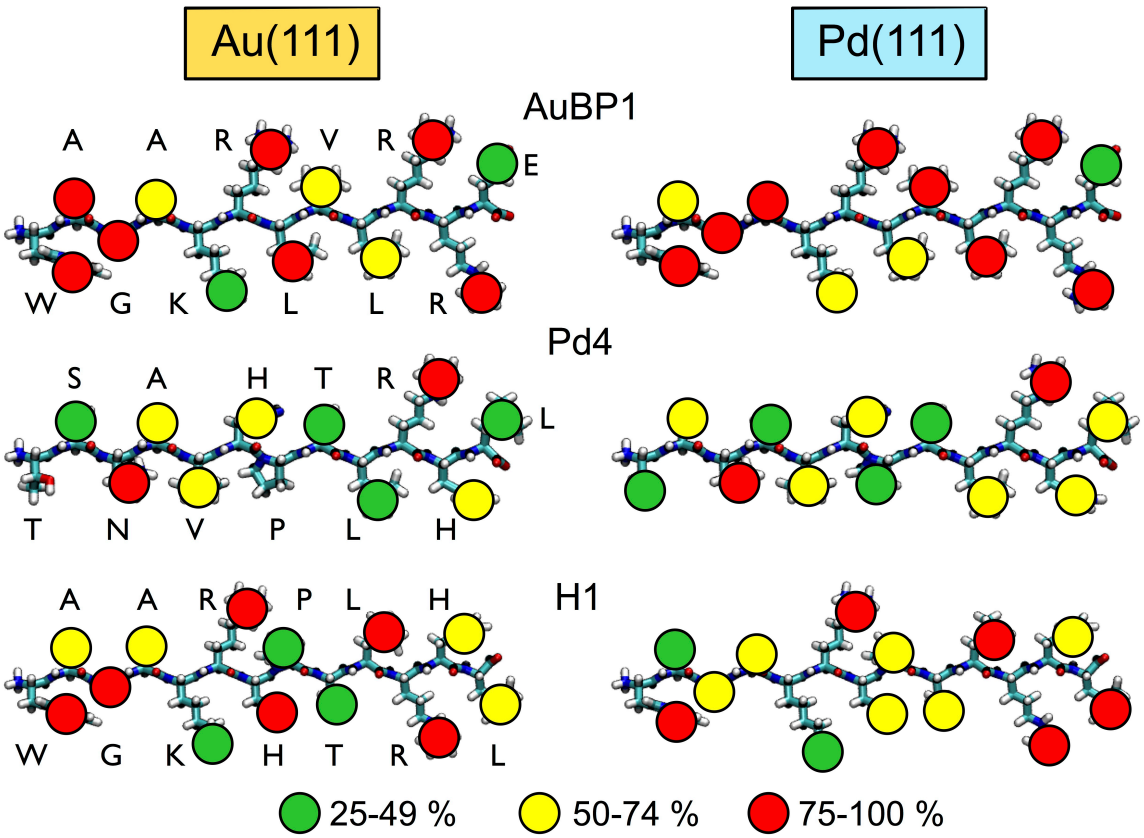

Figure 5: Degree of reside-surface contact for each of the three peptides at the aqueous Au(111) and Pd(111) interfaces determined from the REST-MD simulations.

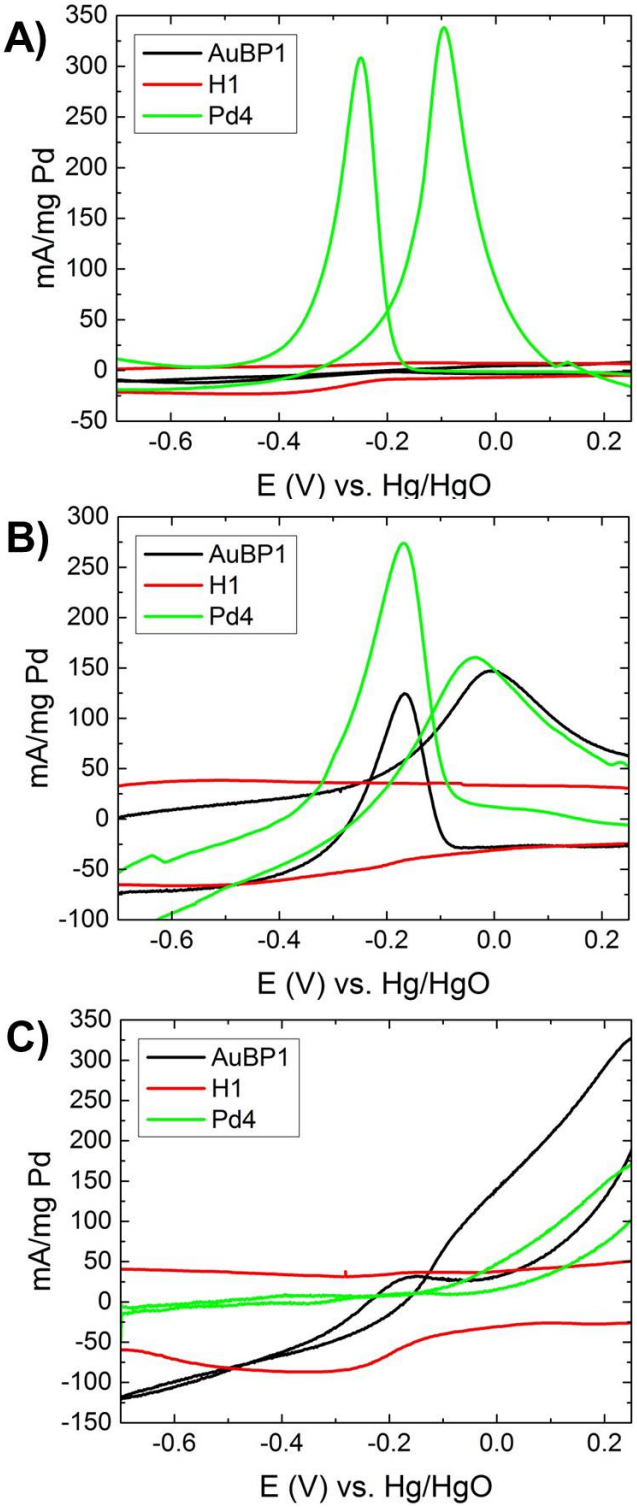

Figure 6: Background subtracted CVs of peptide-caped PdAu bimetallic nanoparticles in 1.0 M NaOH, 1.0 methanol at 20 mV/s for a) 3:1 PdAu; b) 1:1 Pd:Au; and c) 1:3 Pd:Au.

Catalyst	Pd-Pd bond length (Å)	Pd-Au bond length (Å)	Au-Au bond length (Å)	First Atomic-Pair Distance from PDF (Å)
AuBP1 WAGAKRLVLRRE		Pd-Cl bond length (Å)		
Pd	2.74 ± 0.02 Å	2.27 ± 0.20 Å		2.72 Å
3:1 Pd:Au	2.77 ± 0.02 Å	2.80 ± 0.05 Å	2.83 ± 0.01 Å	2.76 Å
1:1 Pd:Au	2.74 ± 0.02 Å	2.79 ± 0.03 Å	2.83 ± 0.02 Å	2.80 Å
1:3 Pd:Au	2.78 ± 0.03 Å	2.83 ± 0.03 Å	2.85 ± 0.02 Å	2.82 Å
Au	-	-	2.88 ± 0.01 Å	2.86 Å
H1 WAGAKRHPTLRHL		Pd-Cl bond length (Å)		
Pd	2.71 ± 0.01 Å	2.30 ± 0.02 Å		
3:1 Pd:Au	2.74 ± 0.02 Å	2.78 ± 0.02 Å	2.80 ± 0.02 Å	
1:1 Pd:Au	2.77 ± 0.05 Å	2.79 ± 0.02 Å	2.81 ± 0.01 Å	
1:3 Pd:Au	2.75 ± 0.01 Å	2.79 ± 0.04 Å	2.85 ± 0.02 Å	
Au	-	-	2.87 ± 0.02 Å	
Pd4 TSNAVHPTLRHL		Pd-Cl bond length (Å)		
Pd	2.76 ± 0.02 Å	2.31 ± 0.09 Å		
3:1 Pd:Au	2.75 ± 0.02 Å	2.79 ± 0.02 Å	2.82 ± 0.01 Å	
1:1 Pd:Au	2.78 ± 0.01 Å	2.81 ± 0.01 Å	2.84 ± 0.01 Å	
1:3 Pd:Au	2.77 ± 0.01 Å	2.81 ± 0.02 Å	2.84 ± 0.01 Å	
Au	-	-	2.84± 0.01 Å	

Table 1. Bimetallic bond lengths obtained from EXAFS modeling of both the Pd K-edge and Au L_3-edge. Note for monometallic Pd, Pd-Cl contributions were used and are also reported.

Catalyst	Pd-Pd CN	Pd-Au CN	Au-Pd CN	Au-Au CN
AuBP1 **WAGAKRLVLRRE**		*Pd-Cl CN*		
Pd	5.51 ± 2.65	*0.80± 0.36*	-	-
3:1 Pd:Au	5.34 ± 1.70	2.93 ± 3.99	4.74 ± 1.47	7.00 ± 5.42
1:1 Pd:Au	2.50 ± 1.46	3.27 ± 1.53	2.91 ± 0.99	5.23 ± 1.28
1:3 Pd:Au	2.06 ± 2.97	6.47 ± 4.77	2.05 ± 1.50	6.51 ± 2.53
Au	-	-	-	9.23 ± 0.72
H1 **WAGAKRHPTLRHL**		*Pd-Cl CN*		
Pd	3.19 ± 0.8	*0.76 ± 0.53*	-	-
3:1 Pd:Au	1.66 ± 1.36	5.37 ± 6.14	4.84 ± 1.03	5.00 ± 3.84
1:1 Pd:Au	1.14 ± 1.03	1.50 ± 2.84	4.23 ± 1.64	4.22 ± 1.81
1:3 Pd:Au	1.52 ± 0.92	6.04 ± 4.69	1.34 ± 1.01	5.79 ± 1.83
Au	-	-	-	9.82 ± 1.17
Pd4 **TSNAVHPTLRHL**		*Pd-Cl CN*		
Pd	4.95 ± 2.37	*0.15 ± 0.36*	-	-
3:1 Pd:Au	4.31 ± 1.19	1.74 ± 0.86	3.76 ± 1.48	5.11 ± 1.78
1:1 Pd:Au	2.98 ± 0.82	3.23 ± 1.41	2.85 ± 0.88	5.81 ± 1.04
1:3 Pd:Au	1.66 ± 1.63	7.80 ± 3.56	2.08 ± 1.19	7.50 ± 1.84
Au	-	-	-	9.76 ± 0.72

Table 2. Bimetallic CNs obtained from EXAFS modeling of both the Pd K-edge and Au L_3-edge. Note for monometallic Pd, Pd-Cl contributions were used and are also reported.

Peptide	Sequence	Surface	No. of anchor residues	S_{conf}	% Surface Pd from RMC simulations		
					3:1 Pd:Au	1:1 Pd:Au	1:3 Pd:Au
AuBP1	WAGAKRLVLRRE	Au(111)	7	2.18	89.0%	66.4%	36.3%
		Pd(111)	8	2.17			
Pd4	TSNAVHPTLRHL	Au(111)	2	2.87	92.2%	73.8%	42.0%
		Pd(111)	2	2.80			
H1	WAGAKRHPTLRHL	Au(111)	6	2.35	100.0%	67.4%	36.3%
		Pd(111)	5	2.31			

Table 3. The number of anchor residues and conformational entropic contributions, $S_{conf,}$ of the peptides adsorbed at the aqueous Au(111) and Pd(111) interfaces, determined from the REST-MD simulations. For comparison, the percentage of surface Pd atoms derived from RMC simulations of atomic PDF and EXAFS modeling results are also provided.

References

1. Tran, P. D.; Wong, L. H.; Barber, J.; Loo, J. S. C. Recent advances in hybrid photocatalysts for solar fuel production. *Energy & Environmental Science* 2012, 5, 5902-5918.
2. Besson, M.; Gallezot, P.; Pinel, C. Conversion of Biomass into Chemicals over Metal Catalysts. *Chem Rev* 2014, 114, 1827-1870.
3. Singh, A. K.; Xu, Q. Synergistic Catalysis over Bimetallic Alloy Nanoparticles. *ChemCatChem* 2013, 5, 652-676.
4. Bandarenka, A. S.; Koper, M. T. M. Structural and electronic effects in heterogeneous electrocatalysis: Toward a rational design of electrocatalysts. *Journal of Catalysis* 2013, 308, 11-24.
5. Ortiz, N.; Weiner, R. G.; Skrabalak, S. E. Ligand-Controlled Co-reduction versus Electroless Co-deposition: Synthesis of Nanodendrites with Spatially Defined Bimetallic Distributions. *ACS Nano* 2014, 8, 12461-12467.
6. Uson, L.; Sebastian, V.; Mayoral, A.; Hueso, J. L.; Eguizabal, A.; Arruebo, M.; Santamaria, J. Spontaneous formation of Au-Pt alloyed nanoparticles using pure nano-counterparts as starters: a ligand and size dependent process. *Nanoscale* 2015, 7, 10152-10161.
7. Liao, H.; Fisher, A.; Xu, Z. J. Surface Segregation in Bimetallic Nanoparticles: A Critical Issue in Electrocatalyst Engineering. *Small* 2015, 11, 3221-3246.
8. Mayrhofer, K. J. J.; Juhart, V.; Hartl, K.; Hanzlik, M.; Arenz, M. Adsorbate-Induced Surface Segregation for Core–Shell Nanocatalysts. *Angewandte Chemie International Edition* 2009, 48, 3529-3531.
9. Lee, S.-Y.; Jung, N.; Cho, J.; Park, H.-Y.; Ryu, J.; Jang, I.; Kim, H.-J.; Cho, E.; Park, Y.-H.; Ham, H. C.; Jang, J. H.; Yoo, S. J. Surface-Rearranged Pd3Au/C Nanocatalysts by Using CO-Induced Segregation for Formic Acid Oxidation Reactions. *ACS Catalysis* 2014, 4, 2402-2408.
10. Dickerson, M. B.; Sandhage, K. H.; Naik, R. R. Protein- and Peptide-Directed Syntheses of Inorganic Materials. *Chem Rev* 2008, 108, 4935-4978.
11. Sarikaya, M.; Tamerler, C.; Jen, A. K. Y.; Schulten, K.; Baneux, F. Molecular Biomimetics: Nanotechnology through Biology. *Nat. Mater.* 2003, 2, 577-585.
12. Mirkin, C. A.; Letsinger, R. L.; Mucic, R. C.; Storhoff, J. J. A DNA-based method for rationally assembling nanoparticles into macroscopic materials. *Nature* 1996, 382, 607-609.
13. Schreiber, R.; Do, J.; Roller, E. M.; Zhang, T.; Schuller, V. J.; Nickels, P. C.; Feldmann, J.; Liedl, T. Hierarchical assembly of metal nanoparticles, quantum dots and organic dyes using DNA origami scaffolds. *Nat Nanotechnol* 2014, 9, 74-78.
14. Schoen, A. P.; Schoen, D. T.; Huggins, K. N. L.; Arunagirinathan, M. A.; Heilshorn, S. C. Template Engineering Through Epitope Recognition: A Modular, Biomimetic Strategy for Inorganic Nanomaterial Synthesis. *J Am Chem Soc* 2011, 133, 18202-18207.
15. Slocik, J. M.; Crouse, C. A.; Spowart, J. E.; Naik, R. R. Biologically Tunable Reactivity of Energetic Nanomaterials Using Protein Cages. *Nano Lett* 2013, 13, 2535-2540.

16. Brown, S.; Sarikaya, M.; Johnson, E. A genetic analysis of crystal growth. *Journal of Molecular Biology* 2000, 299, 725-735.
17. Chiu, C.-Y.; Li, Y.; Ruan, L.; Ye, X.; Murray, C. B.; Huang, Y. Platinum nanocrystals selectively shaped using facet-specific peptide sequences. *Nat Chem* 2011, 3, 393-399.
18. Pacardo, D. B.; Sethi, M.; Jones, S. E.; Naik, R. R.; Knecht, M. R. Biomimetic Synthesis of Pd Nanocatalysts for the Stille Coupling Reaction. *Acs Nano* 2009, 3, 1288-1296.
19. Slocik, J. M.; Naik, R. R. Biologically Programmed Synthesis of Bimetallic Nanostructures. *Advanced Materials* 2006, 18, 1988-1992.
20. Lee, Y.; Kim, J.; Yun, D. S.; Nam, Y. S.; Shao-Horn, Y.; Belcher, A. M. Virus-templated Au and Au-Pt core-shell nanowires and their electrocatalytic activities for fuel cell applications. *Energy & Environmental Science* 2012, 5, 8328-8334.
21. Li, Y.; Tang, Z.; Prasad, P. N.; Knecht, M. R.; Swihart, M. T. Peptide-mediated synthesis of gold nanoparticles: effects of peptide sequence and nature of binding on physicochemical properties. *Nanoscale* 2014, 6, 3165-3172.
22. Coppage, R.; Slocik, J. M.; Sethi, M.; Pacardo, D. B.; Naik, R. R.; Knecht, M. R. Elucidation of Peptide Effects that Control the Activity of Nanoparticles. *Angew Chem Int Edit* 2010, 49, 3767-3770.
23. Coppage, R.; Slocik, J. M.; Ramezani-Dakhel, H.; Bedford, N. M.; Heinz, H.; Naik, R. R.; Knecht, M. R. Exploiting Localized Surface Binding Effects to Enhance the Catalytic Reactivity of Peptide-Capped Nanoparticles. *J Am Chem Soc* 2013, 135, 11048-11054.
24. Bedford, N. M.; Ramezani-Dakhel, H.; Slocik, J. M.; Briggs, B. D.; Ren, Y.; Frenkel, A. I.; Petkov, V.; Heinz, H.; Naik, R. R.; Knecht, M. R. Elucidation of Peptide-Directed Palladium Surface Structure for Biologically Tunable Nanocatalysts. *ACS Nano* 2015, 9, 5082-5092.
25. Bedford, N. M.; Hughes, Z. E.; Tang, Z.; Li, Y.; Briggs, B. D.; Ren, Y.; Swihart, M. T.; Petkov, V. G.; Naik, R. R.; Knecht, M. R.; Walsh, T. R. Sequence-Dependent Structure/Function Relationships of Catalytic Peptide-Enabled Gold Nanoparticles Generated under Ambient Synthetic Conditions. *J Am Chem Soc* 2016, 138, 540-548.
26. Merrill, N. A.; McKee, E. M.; Merino, K. C.; Drummy, L. F.; Lee, S.; Reinhart, B.; Ren, Y.; Frenkel, A. I.; Naik, R. R.; Bedford, N. M.; Knecht, M. R. Identifying the Atomic-Level Effects of Metal Composition on the Structure and Catalytic Activity of Peptide-Templated Materials. *ACS Nano* 2015, 9, 11968-11979.
27. Reiss, B. D.; Mao, C.; Solis, D. J.; Ryan, K. S.; Thomson, T.; Belcher, A. M. Biological Routes to Metal Alloy Ferromagnetic Nanostructures. *Nano Lett* 2004, 4, 1127-1132.
28. Naik, R. R.; Jones, S. E.; Murray, C. J.; McAuliffe, J. C.; Vaia, R. A.; Stone, M. O. Peptide Templates for Nanoparticle Synthesis Derived from Polymerase Chain Reaction-Driven Phage Display. *Adv Funct Mater* 2004, 14, 25-30.
29. Klem, M. T.; Willits, D.; Solis, D. J.; Belcher, A. M.; Young, M.; Douglas, T. Bio-inspired Synthesis of Protein-Encapsulated CoPt Nanoparticles. *Adv Funct Mater* 2005, 15, 1489-1494.

30. Terakawa, T.; Kameda, T.; Takada, S. On easy implementation of a variant of the replica exchange with solute tempering in GROMACS. *J Comput Chem* 2011, 32, 1228-1234.
31. Wright, L. B.; Walsh, T. R. Efficient conformational sampling of peptides adsorbed onto inorganic surfaces: insights from a quartz binding peptide. *Physical Chemistry Chemical Physics* 2013, 15, 4715-4726.
32. Pandey, R. B.; Heinz, H.; Feng, J.; Farmer, B. L.; Slocik, J. M.; Drummy, L. F.; Naik, R. R. Adsorption of peptides (A3, Flg, Pd2, Pd4) on gold and palladium surfaces by a coarse-grained Monte Carlo simulation. *Physical Chemistry Chemical Physics* 2009, 11, 1989-2001.
33. Heinz, H.; Farmer, B. L.; Pandey, R. B.; Slocik, J. M.; Patnaik, S. S.; Pachter, R.; Naik, R. R. Nature of Molecular Interactions of Peptides with Gold, Palladium, and Pd−Au Bimetal Surfaces in Aqueous Solution. *J Am Chem Soc* 2009, 131, 9704-9714.
34. Palafox-Hernandez, J. P.; Tang, Z.; Hughes, Z. E.; Li, Y.; Swihart, M. T.; Prasad, P. N.; Walsh, T. R.; Knecht, M. R. Comparative Study of Materials-Binding Peptide Interactions with Gold and Silver Surfaces and Nanostructures: A Thermodynamic Basis for Biological Selectivity of Inorganic Materials. *Chemistry of Materials* 2014, 26, 4960-4969.
35. Liu, C.-H.; Liu, R.-H.; Sun, Q.-J.; Chang, J.-B.; Gao, X.; Liu, Y.; Lee, S.-T.; Kang, Z.-H.; Wang, S.-D. Controlled synthesis and synergistic effects of graphene-supported PdAu bimetallic nanoparticles with tunable catalytic properties. *Nanoscale* 2015, 7, 6356-6362.
36. Hnilova, M.; Oren, E. E.; Seker, U. O. S.; Wilson, B. R.; Collino, S.; Evans, J. S.; Tamerler, C.; Sarikaya, M. Effect of Molecular Conformations on the Adsorption Behavior of Gold-Binding Peptides. *Langmuir* 2008, 24, 12440-12445.
37. Tang, Z.; Palafox-Hernandez, J. P.; Law, W.-C.; E. Hughes, Z.; Swihart, M. T.; Prasad, P. N.; Knecht, M. R.; Walsh, T. R. Biomolecular Recognition Principles for Bionanocombinatorics: An Integrated Approach To Elucidate Enthalpic and Entropic Factors. *ACS Nano* 2013, 7, 9632-9646.
38. Frenkel, A. I. Applications of extended X-ray absorption fine-structure spectroscopy to studies of bimetallic nanoparticle catalysts. *Chemical Society Reviews* 2012, 41, 8163-8178.
39. Briggs, B. D.; Bedford, N. M.; Seifert, S.; Koerner, H.; Ramezani-Dakhel, H.; Heinz, H.; Naik, R. R.; Frenkel, A. I.; Knecht, M. R. Atomic-scale identification of Pd leaching in nanoparticle catalyzed C-C coupling: effects of particle surface disorder. *Chem Sci* 2015, 6, 6413-6419.
40. Ravel, B.; Newville, M. ATHENA, ARTEMIS, HEPHAESTUS: data analysis for X-ray absorption spectroscopy using IFEFFIT. *J Synchrotron Radiat* 2005, 12, 537-541.
41. Frenkel, A. I.; Nemzer, S.; Pister, I.; Soussan, L.; Harris, T.; Sun, Y.; Rafailovich, M. H. Size-controlled synthesis and characterization of thiol-stabilized gold nanoparticles. *The Journal of Chemical Physics* 2005, 123, -.
42. Beale, A. M.; Weckhuysen, B. M. EXAFS as a tool to interrogate the size and shape of mono and bimetallic catalyst nanoparticles. *Physical Chemistry Chemical Physics* 2010, 12, 5562-5574.

43. Knecht, M. R.; Weir, M. G.; Frenkel, A. I.; Crooks, R. M. Structural Rearrangement of Bimetallic Alloy PdAu Nanoparticles within Dendrimer Templates to Yield Core/Shell Configurations†. *Chemistry of Materials* 2008, 20, 1019-1028.
44. Yevick, A.; Frenkel, A. I. Effects of surface disorder on EXAFS modeling of metallic clusters. *Physical Review B* 2010, 81, 115451.
45. Petkov, V. Nanostructure by high-energy X-ray diffraction. *Mater Today* 2008, 11, 28-38.
46. Keen, D. A.; Mcgreevy, R. L. Structural Modeling of Glasses Using Reverse Monte-Carlo Simulation. *Nature* 1990, 344, 423-425.
47. Sébastien Le, R.; Steve, M.; Randi, C.; Yang, R.; Valeri, P. Three-dimensional structure of multicomponent (Na 2 O) 0.35 [(P 2 O 5) 1 − x (B 2 O 3) x] 0.65 glasses by high-energy x-ray diffraction and constrained reverse Monte Carlo simulations. *Journal of Physics: Condensed Matter* 2011, 23, 035403.
48. Metropolis, N.; Rosenbluth, A. W.; Rosenbluth, M. N.; Teller, A. H.; Teller, E. Equation of State Calculations by Fast Computing Machines. *The Journal of Chemical Physics* 1953, 21, 1087-1092.
49. Huang, W. J.; Sun, R.; Tao, J.; Menard, L. D.; Nuzzo, R. G.; Zuo, J. M. Coordination-dependent surface atomic contraction in nanocrystals revealed by coherent diffraction. *Nat Mater* 2008, 7, 308-313.
50. Kang, J. H.; Menard, L. D.; Nuzzo, R. G.; Frenkel, A. I. Unusual Non-Bulk Properties in Nanoscale Materials: Thermal Metal−Metal Bond Contraction of γ-Alumina-Supported Pt Catalysts. *J Am Chem Soc* 2006, 128, 12068-12069.
51. Krüger, S.; Vent, S.; Nörtemann, F.; Staufer, M.; Rösch, N. The average bond length in Pd clusters Pdn,n=4–309: A density-functional case study on the scaling of cluster properties. *The Journal of Chemical Physics* 2001, 115, 2082-2087.
52. Heinz, H.; Vaia, R. A.; Farmer, B. L.; Naik, R. R. Accurate Simulation of Surfaces and Interfaces of Face-Centered Cubic Metals Using 12−6 and 9−6 Lennard-Jones Potentials. *J. Phys. Chem. C* 2008, 112, 17281-17290.
53. Wright, L. B.; Rodger, P. M.; Corni, S.; Walsh, T. R. GolP-CHARMM: First-Principles Based Force Fields for the Interaction of Proteins with Au(111) and Au(100). *Journal of Chemical Theory and Computation* 2013, 9, 1616-1630.
54. Ozboyaci, M.; Kokh, D. B.; Corni, S.; Wade, R. C. Modeling and simulation of protein–surface interactions: achievements and challenges. *Quarterly Reviews of Biophysics* 2016, 49, e4 (87 pages).
55. Mirau, P. A.; Naik, R. R.; Gehring, P. Structure of Peptides on Metal Oxide Surfaces Probed by NMR. *J Am Chem Soc* 2011, 133, 18243-18248.
56. Wei, F.; Zhang, D.; Halas, N. J.; Hartgerink, J. D. Aromatic Amino Acids Providing Characteristic Motifs in the Raman and SERS Spectroscopy of Peptides. *The Journal of Physical Chemistry B* 2008, 112, 9158-9164.
57. Bower, P. V.; Louie, E. A.; Long, J. R.; Stayton, P. S.; Drobny, G. P. Solid-State NMR Structural Studies of Peptides Immobilized on Gold Nanoparticles. *Langmuir* 2005, 21, 3002-3007.
58. Calle-Vallejo, F.; Koper, M. T. M. First-principles computational electrochemistry: Achievements and challenges. *Electrochimica Acta* 2012, 84, 3-11.
59. *Introduction to Solid State Physics, 8th Edition. Hoboken, NJ: John Wiley & Sons, Inc. 2005*.

60. Vitos, L.; Ruban, A. V.; Skriver, H. L.; Kollár, J. The surface energy of metals. *Surface Science* 1998, 411, 186-202.
61. Wang, L.-L.; Johnson, D. D. Predicted Trends of Core−Shell Preferences for 132 Late Transition-Metal Binary-Alloy Nanoparticles. *J Am Chem Soc* 2009, 131, 14023-14029.
62. Harpeness, R.; Gedanken, A. Microwave Synthesis of Core−Shell Gold/Palladium Bimetallic Nanoparticles. *Langmuir* 2004, 20, 3431-3434.
63. Ferrer, D.; Torres-Castro, A.; Gao, X.; Sepúlveda-Guzmán, S.; Ortiz-Méndez, U.; José-Yacamán, M. Three-Layer Core/Shell Structure in Au−Pd Bimetallic Nanoparticles. *Nano Lett* 2007, 7, 1701-1705.
64. Anderson, R. M.; Yancey, D. F.; Loussaert, J. A.; Crooks, R. M. Multistep Galvanic Exchange Synthesis Yielding Fully Reduced Pt Dendrimer-Encapsulated Nanoparticles. *Langmuir* 2014, 30, 15009-15015.
65. Weiner, R. G.; Kunz, M. R.; Skrabalak, S. E. Seeding a New Kind of Garden: Synthesis of Architecturally Defined Multimetallic Nanostructures by Seed-Mediated Co-Reduction. *Accounts of Chemical Research* 2015, 48, 2688-2695.
66. Wagener, P.; Jakobi, J.; Rehbock, C.; Chakravadhanula, V. S. K.; Thede, C.; Wiedwald, U.; Bartsch, M.; Kienle, L.; Barcikowski, S. Solvent-surface interactions control the phase structure in laser-generated iron-gold core-shell nanoparticles. *Scientific Reports* 2016, 6, 23352.
67. Vu, K. B.; Bukhryakov, K. V.; Anjum, D. H.; Rodionov, V. O. Surface-Bound Ligands Modulate Chemoselectivity and Activity of a Bimetallic Nanoparticle Catalyst. *ACS Catalysis* 2015, 5, 2529-2533.
68. Wasmus, S.; Küver, A. Methanol oxidation and direct methanol fuel cells: a selective review1. *Journal of Electroanalytical Chemistry* 1999, 461, 14-31.
69. Zhao, Y.; Zhan, L.; Tian, J.; Nie, S.; Ning, Z. Enhanced electrocatalytic oxidation of methanol on Pd/polypyrrole–graphene in alkaline medium. *Electrochimica Acta* 2011, 56, 1967-1972.
70. Yin, Z.; Zheng, H.; Ma, D.; Bao, X. Porous Palladium Nanoflowers that Have Enhanced Methanol Electro-Oxidation Activity. *The Journal of Physical Chemistry C* 2009, 113, 1001-1005.
71. Dutta, A.; Datta, J. Outstanding Catalyst Performance of PdAuNi Nanoparticles for the Anodic Reaction in an Alkaline Direct Ethanol (with Anion-Exchange Membrane) Fuel Cell. *The Journal of Physical Chemistry C* 2012, 116, 25677-25688.
72. Liu, Y.; Wang, L.; Wang, G.; Deng, C.; Wu, B.; Gao, Y. High Active Carbon Supported PdAu Catalyst for Formic Acid Electrooxidation and Study of the Kinetics. *The Journal of Physical Chemistry C* 2010, 114, 21417-21422.
73. Brodsky, C. N.; Young, A. P.; Ng, K. C.; Kuo, C.-H.; Tsung, C.-K. Electrochemically Induced Surface Metal Migration in Well-Defined Core–Shell Nanoparticles and Its General Influence on Electrocatalytic Reactions. *ACS Nano* 2014, 8, 9368-9378.
74. Yin, Z.; Chi, M.; Zhu, Q.; Ma, D.; Sun, J.; Bao, X. Supported bimetallic PdAu nanoparticles with superior electrocatalytic activity towards methanol oxidation. *Journal of Materials Chemistry A* 2013, 1, 9157-9163.

75. Hong, W.; Wang, J.; Wang, E. Facile Synthesis of Highly Active PdAu Nanowire Networks as Self-Supported Electrocatalyst for Ethanol Electrooxidation. *ACS Applied Materials & Interfaces* 2014, 6, 9481-9487.
76. Grdeń, M.; Łukaszewski, M.; Jerkiewicz, G.; Czerwiński, A. Electrochemical behaviour of palladium electrode: Oxidation, electrodissolution and ionic adsorption. *Electrochimica Acta* 2008, 53, 7583-7598.
77. Gao, F.; Goodman, D. W. Pd-Au bimetallic catalysts: understanding alloy effects from planar models and (supported) nanoparticles. *Chemical Society Reviews* 2012, 41, 8009-8020.
78. Rehr, J. J.; Mustre de Leon, J.; Zabinsky, S. I.; Albers, R. C. Theoretical x-ray absorption fine structure standards. *J Am Chem Soc* 1991, 113, 5135-5140.
79. Petkov, V. Rad, a Program for Analysis of X-Ray-Diffraction Data from Amorphous Materials for Personal Computers. *J Appl Crystallogr* 1989, 22, 387-389.
80. Orsolya, G.; Valeri, P. Reverse Monte Carlo study of spherical sample under non-periodic boundary conditions: the structure of Ru nanoparticles based on x-ray diffraction data. *Journal of Physics: Condensed Matter* 2013, 25, 454211.
81. Shan, S.; Petkov, V.; Prasai, B.; Wu, J.; Joseph, P.; Skeete, Z.; Kim, E.; Mott, D.; Malis, O.; Luo, J.; Zhong, C.-J. Catalytic activity of bimetallic catalysts highly sensitive to the atomic composition and phase structure at the nanoscale. *Nanoscale* 2015, 7, 18936-18948.
82. Quek, X.-Y.; Filot, I. A. W.; Pestman, R.; van Santen, R. A.; Petkov, V.; Hensen, E. J. M. Correlating Fischer-Tropsch activity to Ru nanoparticle surface structure as probed by high-energy X-ray diffraction. *Chem Commun* 2014, 50, 6005-6008.
83. Le Roux, S.; Petkov, V. ISAACS - interactive structure analysis of amorphous and crystalline systems. *J Appl Crystallogr* 2010, 43, 181-185.
84. Abraham, M. J.; Murtola, T.; Schulz, R.; Páll, S.; Smith, J. C.; Hess, B.; Lindahl, E. GROMACS: High performance molecular simulations through multi-level parallelism from laptops to supercomputers. *SoftwareX* 2015, 1–2, 19-25.
85. MacKerell, A. D.; Bashford, D.; Bellott, M.; Dunbrack, R. L.; Evanseck, J. D.; Field, M. J.; Fischer, S.; Gao, J.; Guo, H.; Ha, S.; Joseph-McCarthy, D.; Kuchnir, L.; Kuczera, K.; Lau, F. T. K.; Mattos, C.; Michnick, S.; Ngo, T.; Nguyen, D. T.; Prodhom, B.; Reiher, W. E.; Roux, B.; Schlenkrich, M.; Smith, J. C.; Stote, R.; Straub, J.; Watanabe, M.; Wiórkiewicz-Kuczera, J.; Yin, D.; Karplus, M. All-Atom Empirical Potential for Molecular Modeling and Dynamics Studies of Proteins. *The Journal of Physical Chemistry B* 1998, 102, 3586-3616.
86. Piana, S.; Laio, A. A bias-exchange approach to protein folding. *Journal of Physical Chemistry B* 2007, 111, 4553-4559.
87. Jorgensen, W. L.; Chandrasekhar, J.; Madura, J. D.; Impey, R. W.; Klein, M. L. Comparison of simple potential functions for simulating liquid water. *The Journal of Chemical Physics* 1983, 79, 926-935.
88. Neria, E.; Fischer, S.; Karplus, M. Simulation of activation free energies in molecular systems. *The Journal of Chemical Physics* 1996, 105, 1902-1921.
89. Ertem, S. P.; Tsai, T.-H.; Donahue, M. M.; Zhang, W.; Sarode, H.; Liu, Y.; Seifert, S.; Herring, A. M.; Coughlin, E. B. Photo-Cross-Linked Anion Exchange Membranes with Improved Water Management and Conductivity. *Macromolecules* 2016, 49, 153-161.

90. Tsai, T.-H.; Ertem, S. P.; Maes, A. M.; Seifert, S.; Herring, A. M.; Coughlin, E. B. Thermally Cross-Linked Anion Exchange Membranes from Solvent Processable Isoprene Containing Ionomers. *Macromolecules* 2015, 48, 655-662.
91. Ye, J.; Liu, J.; Xu, C.; Jiang, S. P.; Tong, Y. Electrooxidation of 2-propanol on Pt, Pd and Au in alkaline medium. *Electrochemistry Communications* 2007, 9, 2760-2763.
92. Renjith, A.; Lakshminarayanan, V. One step preparation of 'ready to use' Au@Pd nanoparticle modified surface using deep eutectic solvents and a study of its electrocatalytic properties in methanol oxidation reaction. *Journal of Materials Chemistry A* 2015, 3, 3019-3028.